Research Article BEU Fen Bilimleri Dergisi 15(3): 1159-1182 (2026) DOI: 10.17798/bitlisfen.1869499

BİTLİS EREN UNIVERSITY
FEN BİLİMLERİ DERGİSİ
ISSN: 2147-3129 / e-ISSN: 2147-3188

SEISMICITY PARAMETERS OF THE WESTERNMOST PART OF THE NORTH ANATOLIAN FAULT ZONE (NAFZ)

Burçin Didem TAMTAŞ

Istanbul University-Cerrahpasa, Faculty of Engineering, Department of Geophysical Engineering, Istanbul, Türkiye,
burcin.tamtas@iuc.edu.tr

Article Info

Received: *January 22, 2026*
Revised: *March 7, 2026*
Accepted: *March 25, 2026*

Keywords
North Anatolian Fault Zone,
Saros Segment,
b-value,
Stress Tensor Inversion,
Transtensional Tectonics,
Seismicity Parameters.

ABSTRACT

This study characterizes seismicity and stress regime in the westernmost part of the North Anatolian Fault Zone (NAFZ), focusing on the Saros segment, where dextral strike-slip deformation transitions into the transtensional northern Aegean domain. Unlike previous regional studies that combine Marmara and broader Aegean datasets or focus on individual rupture sequences, this study isolates a coordinate-bounded transition window to quantify the intrinsic seismic behavior of the terminal NAFZ–North Aegean Trough (NAT) linkage zone within a completeness-controlled framework. A December 1917–September 2025 earthquake catalog was compiled and homogenized to local magnitude (ML). Completeness analysis yields a reference Mc ≈ 3.2, consistent with Gutenberg–Richter statistics. Recurrence and annual probability metrics were evaluated for 1917–2025, 1985–2025, and 2010–2025 to assess temporal stability and completeness-related effects in seismic productivity. Recurrence and frequency–magnitude characteristics of the non-declustered and declustered catalogs were compared to assess aftershock effects on seismic rates. For events with M ≥ Mc, the estimated parameters are b = 0.91 ± 0.05 and a = 5.392 indicate moderate seismic productivity. Focal mechanisms and stress tensor inversion indicate a dominant dextral strike-slip regime with subordinate N–S extension, confirming a transtensional stress field linking the Saros region to the northern Aegean. Integrated completeness-controlled seismicity statistics and stress-tensor inversion show that the Saros segment functions as a transform–transtensional linkage corridor rather than a discrete tectonic boundary, refining the seismotectonic framework of the Marmara–Saros–North Aegean transition zone and providing robust parameters for seismic hazard and fault-segmentation analyses.

1. INTRODUCTION

The NAFZ constitutes a principal right-lateral, intracontinental transform boundary in Türkiye, extending from the Karlıova triple junction—where it meets the left-lateral East Anatolian transform—to the Saros Gulf in the west. This fault zone produced a westward-migrating sequence of large earthquakes during the twentieth century [1-5]. The 26 December 1939 Erzincan earthquake (M_s=7.9) is described as the largest event along the NAFZ, and subsequent large earthquakes are widely reported to have migrated westward along the fault zone [6-11]. This progression is commonly discussed in the context of earthquake interaction and stress triggering, which successive ruptures promote failure of adjacent segments to the west [12, 13]. Within this context, the western end of the NAFZ is of particular interest because it represents the terminal part of a major transform system and coincides with the Marmara–northern Aegean transition, where fault geometry, segmentation, and deformation style become increasingly complex [14].

In this study, “the westernmost part of the NAFZ” refers to the terminal segment of the fault system within a coordinate-bounded transition window in the Saros segment of the North Aegean Trough (NAT) (40.25–40.55°N, 25.8–26.7°E), where NAFZ-related dextral shear interacts with a transtensional regime

 License: CC BY-NC 4.0

as the fault system transitions into the NAT [14]. This window is intentionally restricted and does not represent the entire Gulf of Saros (Figure 1).

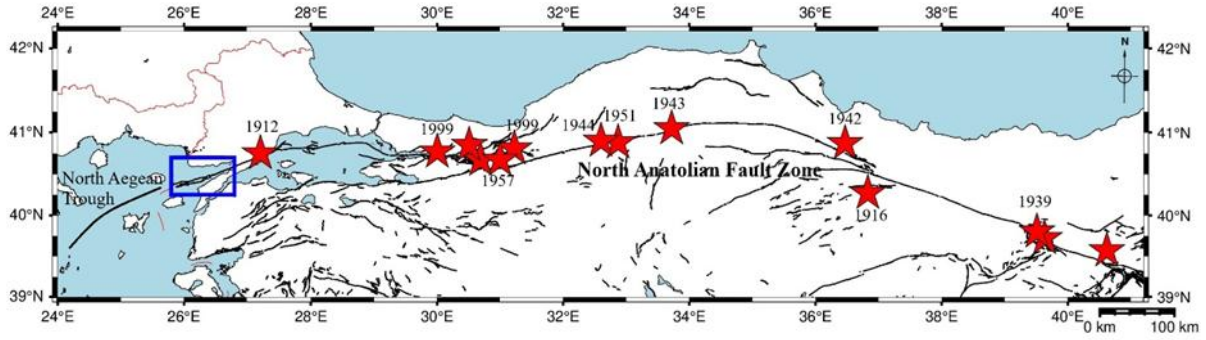


Figure 1. The westward migration of major destructive earthquakes along the NAFZ (The study area is shown with a blue square). The map was created by the author using fault systems based on [15] via Generic Mapping Tools GMT 6.6 [16].

NAT is commonly interpreted as the offshore continuation of the North Anatolian Fault (NAF) system toward the Aegean domain, and its kinematics reflect a combination of right-lateral shear and extension, often framed in terms of transtension and strain partitioning [14, 17-19]. Focal mechanisms further support a regional contrast, with largely strike-slip solutions beneath the Sea of Marmara and strike-slip/normal faulting with NE–SW tensional axes beneath the Aegean, motivating segment-scale mapping and barrier identification for realistic earthquake scenarios [6].

The Saros segment has been identified as a key link between the Sea of Marmara and the NAT. The 1912 Mürefte (Ganos) earthquake (M_s=7.3) sequence provides important constraints on the westernmost inland section of the NAFZ and its connection toward the Marmara–Saros–NAT system [14, 20-23]. Paleoseismological synthesis emphasizes that the Ganos segment is bounded by offshore fault segments to the east (the Sea of Marmara) and to the west (Saros/NAT), underscoring the relevance of the terminal region for seismic-hazard considerations [21, 22, 24, 25]. In addition, the July 2003 earthquake sequence has been interpreted as activating a ~25 km-long zone along the northern edge of the Saros depression with nearly pure dextral strike-slip mechanisms, consistent with the westward continuation of the NAFZ northern branch into the Saros segment and the NAT [4]. Recent work has also highlighted the importance of mapping subaqueous fault scarps and offshore traces to constrain seismic gaps, segment boundaries, and possible offshore rupture extensions near the Marmara and Saros [12, 26, 27].

Robust characterization of seismicity in such an offshore transition zone requires careful treatment of catalog heterogeneity, completeness (M_c), and clustering, since spatial/temporal variations in monitoring and magnitude reporting may bias frequency–magnitude statistics if not explicitly addressed [28, 29]. Accordingly, the seismicity parameters of the westernmost NAFZ are quantified here using a homogenized earthquake catalog and a consistent workflow that includes magnitude conversions, declustering, estimation of M_c and Gutenberg–Richter parameters, and recurrence/annual probability metrics. The resulting Gutenberg–Richter parameters (a and b) are interpreted in the context of published constraints on segmentation and deformation style across the Marmara–NAT transition. In addition, focal mechanism solutions are incorporated to assess consistency with the mixed strike-slip/transtensional regime reported for the region. The resulting completeness-aware, homogenized, and declustered parameterization provides a focused basis for discussing along-strike heterogeneity and segment-scale behavior near the terminal part of the NAFZ.

Extensive research has significantly improved understanding of the western North Anatolian Fault Zone (NAFZ), particularly through structural mapping, paleoseismological investigations of the Ganos segment, and detailed analyses of major earthquake sequences, including the 1912 and 2003 events. These studies have provided essential constraints on fault geometry, rupture behavior, and regional tectonic evolution.

Building on this foundation, the present study adopts a spatially focused, completeness-aware seismicity framework to examine the Saros sector as a defined transition window between the NAFZ and the North Aegean Trough (NAT). The analysis integrates long-term magnitude–frequency scaling, temporal evolution of completeness, recurrence modeling, focal-mechanism classification, and stress tensor inversion within the same restricted domain.

Through this integrated perspective, the Saros segment is interpreted as a mechanically transitional transform–transtensional linkage zone. The near-unity b-values, stable recurrence characteristics, and stress ratio ($R \approx 0.47$) collectively indicate a balanced strike-slip regime modulated by subordinate N–S extension, providing a quantitative mechanical context for understanding transform termination and strain partitioning at the western end of the NAFZ.

2. SEISMOTECTONIC and SEISMICITY SETTING

The study area is located at the westernmost part of the NAFZ, within a coordinate-bounded transition window (40.25–40.55°N, 25.8–26.7°E) at Saros, at the easternmost part of the North Aegean Trough (NAT). This window is intentionally restricted and does not represent the entire Gulf of Saros. In a broader tectonic sense, the NAT is widely interpreted as the Aegean continuation of the NAF system across western Türkiye and the Marmara region, and its deformation reflects a combination of right-lateral shear and extension. In the eastern part of the trough and in the Gulf of Saros, dextral displacement has been documented from marine geophysical observations [22, 30]. At the same time, strain partitioning in the shallow crust is described to allow two styles of faulting to coexist—transtensional basin-bounding faults and dextral faulting within the basin—supported by earthquake focal mechanisms [14].

At the local scale, seismological observations provide essential constraints on the active deformation within the Saros depression. Analysis of the July 2003 earthquake sequence (M_w 5.7), using precise event locations and source properties, indicated activation of an approximately 25 km-long zone along the northern margin of the Saros depression [4]. The focal mechanisms solutions of the event and the largest aftershocks suggest nearly pure dextral strike-slip faulting. In contrast, the southern boundary fault of the Gulf of Saros is interpreted as a normal fault based on seismic sections [31]. Consequently, the principal deformation zone is inferred to comprise a major strike-slip fault near the northern margin of the Saros depression, considered a continuation of the north branch of the NAF into the Saros–NAT domain [4, 22].

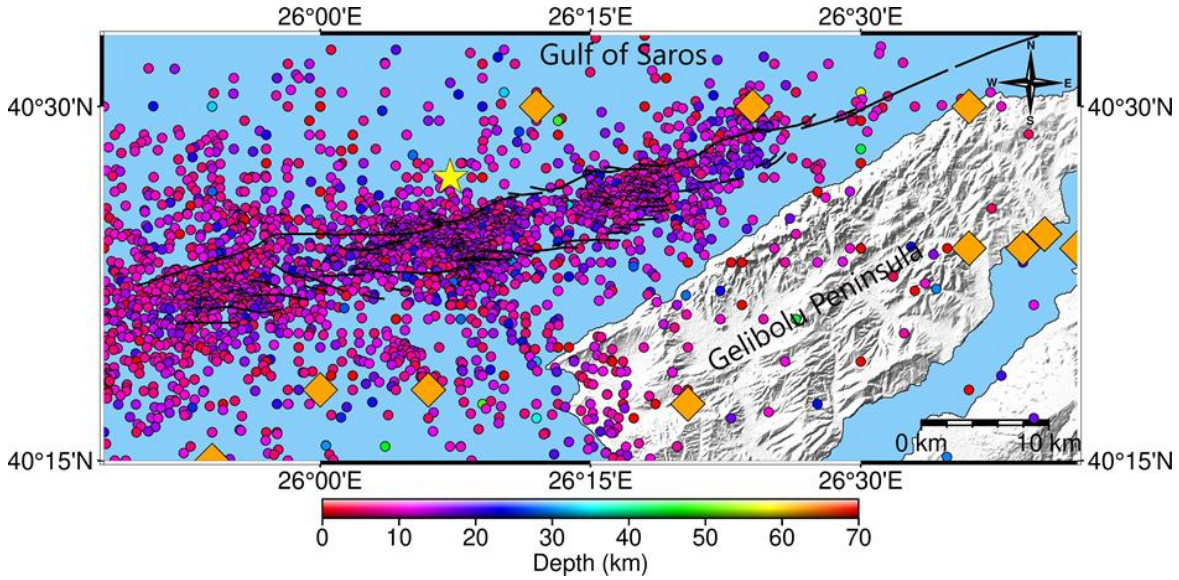


Figure 2. Seismicity map of the study area. Epicenters are color-coded by depth; orange diamonds indicate historical earthquakes compiled from the AFAD historical earthquake catalog. The yellow star denotes the 27 March 1975 event (M_L 5.7). Fault traces and fault names correspond to the Saros Segment and the northern branch of the North Anatolian Fault Zone (NAFZ), as defined by Emre, et al. [15] and Aksoy, et al. [12].

Historical seismicity further indicates that the westernmost segment of the NAFZ has repeatedly produced damaging earthquakes. The 9 August 1912 Mürefte (Ganos) (M_s=7.3) earthquake is described as being generated on the Ganos fault, identified as one of the westernmost segment of the North Anatolian fault, with additional constraints provided by coseismic slip, segmentation, and historical records; a second major shock on 13 September 1912 is reported to have occurred farther west near Saros Bay, close to the western end of the 9 August rupture [21]. A regional paleoseismological compilation of historical earthquakes in the Ganos region includes several large events (e.g., 484 M_s 7.2; 1063 M_s 7.4; 1354 M_s 7.4; 1659 M_s 7.2; 1766 M_s 7.4) (Figure 2), highlighting the long-term recurrence of strong shaking in the wider Marmara–Saros segment [24].

A summary of historical earthquakes affecting the Saros–Ganos segment, including their approximate epicentral coordinates and maximum reported intensities (MMI), is provided in Table 1.

Table 1. Historical earthquakes affecting the Saros–Ganos segment compiled from the Disaster and Emergency Management Authority of Türkiye (AFAD) historical earthquake catalog. Reported values correspond to the maximum observed Modified Mercalli Intensity (MMI). Coordinates represent approximate epicentral locations as provided in the catalog. Dates are given in CE (Common Era) and BCE (Before Common Era).

Year	Date	Latitude (°N)	Longitude (°E)	Maximum Intensity (MMI)	Location
360 BCE	—	40.4	26.6	IX	Hellespont (Çanakkale Strait)
484 CE	—	40.5	26.6	IX	Gelibolu–Bozcaada
1625 CE	18. May	40.3	26	X	Saros
1659 CE	17. Feb	40.5	26.4	IX	Saros
1846 CE	19. Sep	40.4	26.65	VI	Gelibolu
1847 CE	04. Jul	40.4	26.65	VI	Gelibolu
1852 CE	04. Apr	40.41	26.67	VI	Çanakkale
1855 CE	17. Mar	40.41	26.67	V	Gelibolu
1859 CE	18. Aug	40.25	25.9	IX	Thessaloniki (Greece)
1859 CE	21. Aug	40.3	26.1	IX	Saros Gulf–Imbros
1867 CE	20. Mar	40.41	26.67	VII	Gelibolu
1871 CE	08. Oct	40.4	26.7	VII	Thrace
1873 CE	13.Jan	40.4	26.7	VII	Saros–Gelibolu–Çanakkale–Tekirdağ–Imbros–Samothraki
1881 CE	04. Oct	40.4	26.7	VI	Gelibolu
1893 CE	09. Feb	40.5	26.2	IX	Saros
1895 CE	04. Mar	40.4	26.7	V	Saros Gulf

In the instrumental period, seismicity within the study window is characterized predominantly by small-to-moderate magnitude earthquakes concentrated offshore along the northern margin of the Saros depression. Hypocentral depths are mainly confined to the upper crust (0–20 km), consistent with brittle deformation along the northern branch of the North Anatolian Fault Zone (NAFZ).

The largest instrumental earthquake within the study area is the 27 March 1975 event (05:15:07.90; 40.4500°N, 26.1200°E) with M_L 5.7, while regional compilations report magnitudes of approximately M_s 6.6 for the same event [24]. In addition, the 6 July 2003 strike-slip sequence (M_w 5.7) along the northern margin of the Saros depression further confirms the dominance of dextral strike-slip faulting in the region [4, 32].

Overall, instrumental seismicity indicates persistent moderate activity distributed along a structurally complex transition zone where strike-slip deformation associated with the westernmost NAFZ interacts with transtensional structures of the northern Aegean domain. The predominance of shallow events and the absence of very large instrumental earthquakes within the study window are consistent with the segmented and mechanically transitional character of this terminal fault segment.

3. DATA and METHODS

3.1. Data

The earthquake dataset was compiled for the study area (40.25–40.55°N, 25.8–26.7°E) and covers the period from December 1917 to September 2025 (based on the latest available update of the Kandilli Observatory and Earthquake Research Institute (KOERI) catalog, accessed in January 2026). Instrumental seismicity was extracted from the KOERI catalog. For each event, reported magnitude type(s) (e.g., M_L, M_D, M_b, M_s, M_w) were retained. Given that this study aims to characterize regional seismicity parameters—including microseismicity—within a small spatial window, the compiled dataset is dominated by small-to-moderate events, most consistently reported in the KOERI catalog as local magnitude (M_L). In such settings, converting the entire dataset to M_w would rely heavily on empirical conversions, typically calibrated over limited magnitude ranges and less constrained at lower magnitudes that control catalog completeness. Accordingly, M_L was adopted as the reference magnitude to maximize data coverage and to avoid introducing additional conversion-driven epistemic uncertainty into subsequent analyses.

Historical earthquake information was compiled from the AFAD historical catalog and used to provide long-term context for regional seismicity and to highlight major damaging events affecting the wider Marmara–Saros segment.

Focal mechanism information was compiled from multiple global and regional resources, including the AFAD catalog, the Global Centroid Moment Tensor (GCMT) database, the Regional Centroid Moment Tensor (RCMT) catalog, and solutions available through the International Seismological Centre (ISC), complemented by mechanisms reported in the published literature [33-36].

3.2. Methodology

3.2.1. Magnitude Homogenization and Conversion Relations

To ensure consistency across mixed-magnitude reporting while preserving the microseismicity content of the KOERI catalog, all magnitudes were homogenized to the local magnitude (M_L), which provides the highest coverage in the study window. Because catalog completeness (M_c) and the Gutenberg–Richter b-value are predominantly controlled by the low-to-moderate-magnitude range, adopting the most densely populated and operationally stable scale is essential to minimize conversion-driven artefacts. A direct homogenization to M_w was not pursued because M_w observations are sparse in the window, and empirical M_w conversions are generally calibrated over restricted magnitude ranges, increasing uncertainty at the small magnitudes that dominate completeness and b-value estimation. Accordingly, M_L was retained as a single reference scale to avoid introducing additional epistemic uncertainty and potential bias into the M_c and b estimates. Magnitude conversion relations between M_L and other reported magnitude scales were derived using General Orthogonal Regression (GOR), which accounts for measurement uncertainties affecting both the response and predictor variables [37-39]. The linear model was used to express the conversion (Equation 1),

$$M_L = a + bM_x \tag{1}$$

Where Mx denotes the original magnitude type, and a and b are the intercept and slope, respectively. Within the GOR framework, the error variance ratio (λ) and the orthogonal standard deviation ($\sigma\perp$) were used to characterize dispersion around the regression line, and the Pearson correlation coefficient (R) was reported to describe the linear association [37, 39, 40]. The homogenized catalog served as the basis for subsequent statistical analyses.

Although local magnitude (M_L) is known to exhibit saturation effects at moderate-to-large magnitudes (typically around $M_L \approx 5.5$–6.0), the observed magnitude range in this study is dominated by small-to-moderate events ($M_c = 3.2$ to $M_L \approx 5.7$), which primarily control the estimation of the Gutenberg–Richter slope and completeness threshold. Within this interval, M_L provides the most internally consistent and best-constrained magnitude scale available for the study window. Recurrence estimates extending toward $M_L \approx 6.0$–6.5 are based on extrapolation of the fitted Gutenberg–Richter relation and should therefore be interpreted cautiously, particularly in view of potential M_L saturation effects near the upper

magnitude bound. Accordingly, the use of M_L is considered methodologically appropriate for completeness and b-value estimation within the observed magnitude range.

3.2.2. Catalog Declustering

Before estimating seismicity parameters, the catalog was declustered to reduce the influence of dependent events (foreshocks/aftershocks) and better represent background seismicity. Declustering was performed using the Reasenberg [41] approach, as implemented in ZMAP V. 7.1 software [42], with the parameter set to a 1-day minimum look-ahead window for events treated as independent and a 10-day maximum look-ahead window for clustered activity, a confidence level of 0.95, an XK factor of 0.5, an interaction radius factor of 10, an effective minimum magnitude cutoff of 1.5, an epicentral error of 1.5 km, and a depth error of 2 km. Clusters were not replaced by an equivalent event. All calculations and Gutenberg–Richter analyses were conducted using the declustered catalog, unless explicitly stated otherwise.

3.2.3. Gutenberg–Richter Frequency–Magnitude Relation

For magnitudes exceeding the completeness threshold (M_c), the earthquake-size distribution was modeled using the cumulative Gutenberg–Richter relation [43] as expressed in Equation 2:

$$\log_{10} N(M \geq m) = a - bM \tag{2}$$

Where N ($M \geq m$) denotes the cumulative number of events with a magnitude of at least m, a represents the level of seismic productivity over the observation period, and b indicates the ratio of small to large earthquakes. Variations in b have been linked to differences in crustal heterogeneity and stress conditions [44-46]. While b is typically near 1.0 across many tectonic environments, it may deviate from this value depending on regional conditions [47].

b-values were estimated for events with $M \geq M_c$ using a maximum-likelihood approach [48], as implemented in ZMAP V.7.1 [42]. The estimator was expressed in Equation 3:

$$b = \frac{\log_{10} e}{\bar{M} - (M_c - \frac{\Delta M}{2})} \tag{3}$$

Where is $\bar{M}$ the mean magnitude of events with $M \geq M_c$, and ΔM is the magnitude bin size.

3.2.4. Recurrence and Annual Probability

In this study, earthquake recurrence intervals and annual probabilities were computed using the Poisson model described below. The Poisson model estimates the probability of observing at least one earthquake of a specified magnitude within a defined time interval and geographic region [49]. This model is widely used in probabilistic seismic hazard analysis because it is well-suited to modeling rare, independent events over time [50, 51].

The recurrence period, also known as the return period, denotes the expected average interval between earthquakes that exceed a specified magnitude threshold. This period is estimated as the inverse of the annual probability rate (λ) (Equation 4):

$$T_r = 1/\lambda \tag{4}$$

After determining the event rate (λ) for a given magnitude range, the probability of observing at least one earthquake of magnitude $\geq M$ within a specified time window t can be calculated using the Poisson distribution [49] as expressed in Equation 5:

$$P(t) = 1 - e^{-\lambda t} \tag{5}$$

Unless otherwise stated, recurrence and probability estimates were computed using the declustered catalog to better satisfy the temporal independence assumption. For comparison, recurrence and annual

probability curves were also computed for the original (non-declustered) 1917–2025 catalog to explicitly assess the impact of clustering on long-term rate estimates.

In this study, the recurrence and probability analyses were performed separately for three time windows (1917–2025, 1985–2025, and 2010–2025). This multi-window approach allows evaluation of how catalog completeness and network improvements affect the derived recurrence intervals and annual probabilities across different observation periods.

3.2.5. Focal-Mechanism Visualization and Ternary (P–T–B) Representation

The classification and visualization of large datasets of focal mechanisms are essential for effectively illustrating complex faulting mechanisms. Frohlich and Apperson [52] introduced a diagram for classifying focal mechanisms by rupture type; however, this representation exhibits distortions at its extremes. Kagan [53] addressed these limitations by defining the diagram's boundaries using the Kaverina, et al. [54] projection with great circles, forming a triangle to minimize distortions and dividing the octant into three categories: normal, reverse, and strike-slip. Although Kagan's approach is straightforward, it may not provide sufficient detail for comprehensive seismotectonic analyses. The present study employs the FMC program to classify earthquake focal mechanisms with greater detail using double-couple (DC) rupture types [55]. FMC goes beyond the primary faulting mechanisms by treating mixed/transition solutions—such as normal–strike-slip and strike-slip–reverse—separately, thereby providing a finer seven-class classification scheme [56].

3.2.6. Stress Tensor Inversion

A regional stress tensor was estimated from the focal mechanism dataset through stress inversion. The Michael method [57, 58] was applied to stress-tensor inversion to determine the principal stress axes (σ_1, σ_2, and σ_3) and the best-fitting stress tensor for the focal-mechanism dataset [59]. Here, σ_1 denotes the maximum compressive stress, σ_2 the intermediate stress, and σ_3 the minimum compressive stress. The relative orientation of these axes defines the tectonic regime. A vertical orientation of σ_1 characterizes an extensional tectonic setting. A vertical σ_2 is indicative of a strike-slip regime. A vertical σ_3 suggests a compressional (thrust) regime. The shape ratio R is defined in Equation 6:

$$R = \frac{\sigma_2 - \sigma_1}{\sigma_3 - \sigma_1} \tag{6}$$

The shape ratio R was determined by minimizing the misfit between the observed slip directions and those predicted by the trial stress tensor [57, 58]. Because focal mechanisms provide two nodal planes, the inversion workflow incorporated a resampling/selection procedure to identify the fault plane that best fits the stress model within each bootstrap realization [60]. The shape ratio was defined as with R constrained between 0 and 1.

The inversion was implemented using the STRESSINVERSE package [61]. Uncertainty in the inferred stress axes was evaluated using bootstrap resampling, and confidence regions for the principal axes were reported alongside the best-fitting orientations. Although the number of mechanisms (N = 33) is moderate, the bootstrap procedure was applied to assess the robustness and stability of the inferred principal stress orientations. The inversion outputs include (i) azimuth/plunge of σ1, σ2, and σ3; (ii) the distribution of axis orientations across bootstrap solutions; and (iii) the distribution and best estimate of the shape ratio R. The shape ratio R provides a compact measure of the relative magnitudes of the principal stresses and is commonly used to summarize the stress regime in combination with axis orientations [62].

4. RESULTS and DISCUSSION

The analysis covers the period from December 1917 to September 2025 and includes 2855 earthquakes located within the study area (40.25–40.55°N, 25.8–26.7°E). The selected window represents the westernmost transition zone of the NAFZ at Saros, where dextral strike-slip deformation interacts with transtensional structures of the northern Aegean domain. The spatial limits were intentionally defined to emphasize local seismicity and minimize the influence of adjacent regions such as the Marmara and central Aegean domains, which display distinct seismotectonic characteristics. This focused spatial

design ensures that the derived seismic parameters reflect the intrinsic behavior of the terminal NAFZ–NAT linkage zone rather than broader regional trends.

Before the seismicity and statistical evaluations, the earthquake catalog—containing events reported in multiple magnitude scales—was homogenized to a single reference scale to ensure consistency across the dataset. Magnitudes reported as M_D and M_b were converted to local magnitude (M_L) using empirical conversion relations derived for the study area, as described in the Data and Methods section. The resulting regression parameters and calibration ranges are summarized in Table 2.

Table 2. General-orthogonal-regression (GOR)–based magnitude conversion relations are used to homogenize the catalog to the local magnitude (M_L). For each relation, the number of paired observations (N), Pearson correlation coefficient (R), orthogonal standard deviation (σ⊥), and the calibration ranges (min–max) of the paired magnitudes (Mx and M_L) are reported.

M_L = b0 + b1*Mx	N	R	σ⊥	Mx range (min–max)	M_L range (min–max)
M_L=0.0889+0.9874*M_D	35	0.99	0.07	M_D: 1.6–4.5	M_L: 1.7–4.5
M_L=0.2428+0.9501*M_b	37	0.87	0.18	M_b: 2.3–5.3	M_L: 2.4–5.3

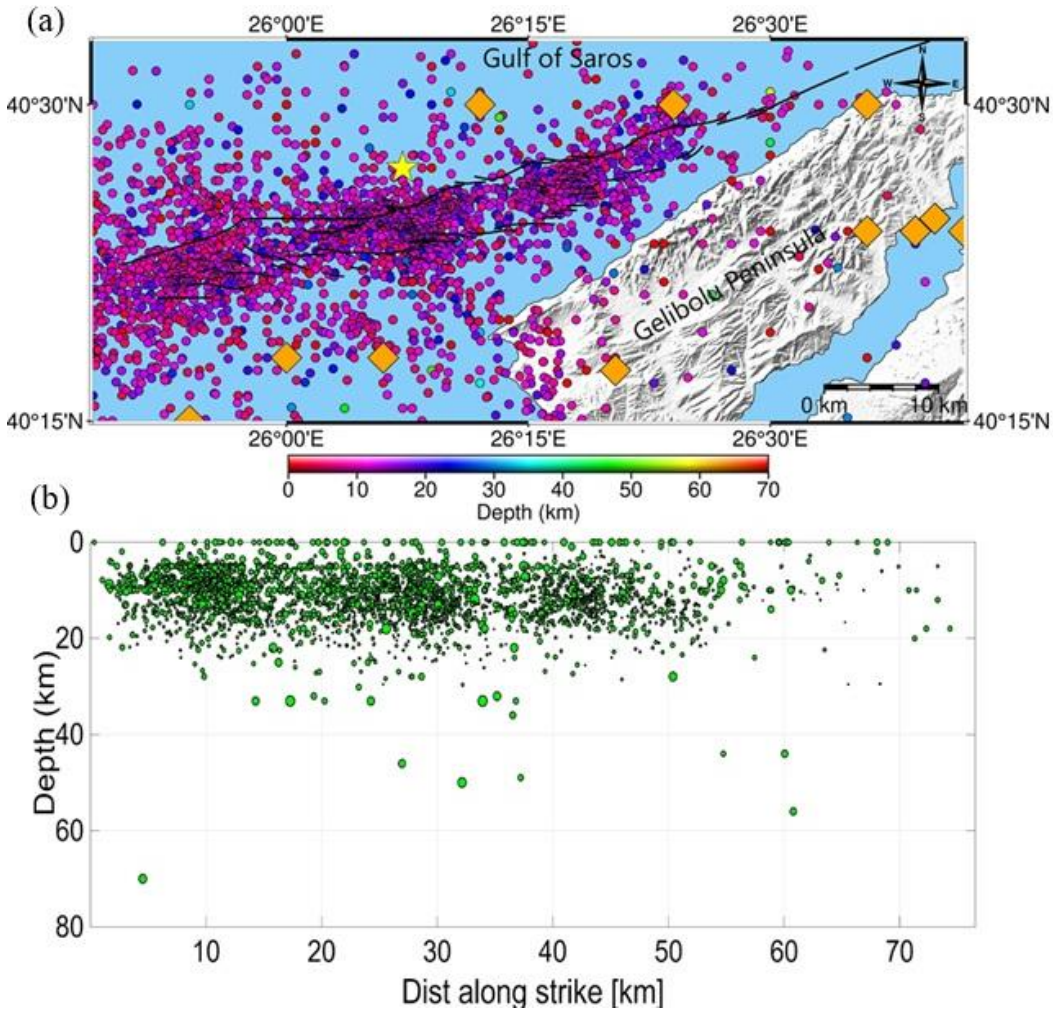


Figure 3. (a) Seismicity map of the study area with earthquake epicenters color-coded by focal depth (km). Orange diamonds show historical earthquakes, and a yellow star indicates the 27 March 1975 event (M_L 5.7). Fault traces and fault names correspond to the Saros Segment and the northern branch of the North Anatolian Fault Zone (NAFZ) and as defined by Emre, et al. [15] and Aksoy, et al. [12]. Historical and instrumental earthquake parameters are consistent with those presented in Figure 2. (b) Focal depth plotted against distance along strike for the same earthquake catalog.

In total, 2855 events were analyzed in the homogenized M_L catalog, including 2102 originally reported as M_L and 753 converted from other magnitude types (M_D: 650; M_b: 103). The homogenized M_L dataset was subsequently used for completeness analysis and Gutenberg–Richter parameter estimation, as detailed in the following sections.

Figure 3a illustrates the spatial distribution of earthquake epicenters within the study area, color-coded by focal depth. The epicentral pattern reveals several dense offshore clusters, while onshore activity is comparatively sparse. Most hypocenters occur at shallow depths (0–20 km), consistent with deformation confined to the brittle upper crust. A smaller number of events extend to intermediate depths of ~20–40 km, and earthquakes deeper than ~40 km are uncommon. The largest instrumental event in the region, the 27 March 1975 earthquake (M_L 5.7; yellow star), lies within the main offshore seismicity belt. Historical earthquakes, shown as orange diamonds, are spatially consistent with the offshore trend, suggesting long-term persistence of the main seismogenic zone. Mapped fault traces (black lines) broadly coincide with these clusters, supporting their association with the NAFZ's northern branch.

Figure 3b shows the depth distribution along strike. Hypocenters are dominantly concentrated in the upper crust throughout the profile, with only a limited number extending to ~50–70 km. Deep events (>40 km) are few and may be affected by location uncertainty in the earlier catalog; therefore, the depth interpretation focuses on the dominant 0–20 km population. The scarcity of deeper events indicates that the active seismogenic layer beneath the Saros–NAT transition is relatively thin, which is consistent with other studies reporting crustal thicknesses of ~30 km and predominantly shallow slip behavior in the western NAFZ and the northern Aegean regions [4, 14] This concentration of seismicity within the upper crust suggests that strain release is accommodated mainly by brittle faulting rather than distributed deformation at depth, reflecting the mechanically segmented nature of the westernmost NAFZ.

Figure 4 shows the magnitude–frequency histogram of the analyzed catalog using a bin size of 0.1 magnitude units. The distribution is dominated by low magnitudes, with most earthquakes concentrated between approximately $M_L \approx 1.0$ and 3.5. Event frequency decreases progressively with increasing magnitude, and only a limited number of earthquakes exceed $M_L \approx 4.0$, with very few reaching $M_L \approx 5.7$. This pattern reflects both the natural frequency–magnitude relationship typical of active fault systems and the influence of detection capability, since smaller events are more readily recorded in recent decades as seismic network coverage and sensitivity have improved. The relatively low number of larger events is consistent with the moderate seismic productivity expected for a localized fault-bounded domain such as the Saros segment of the NAFZ. Overall, the magnitude distribution indicates that the catalog adequately captures the small- and moderate-magnitude activity required for reliable estimation of b-values and recurrence statistics. However, the limited number of high-magnitude events constrains the upper-magnitude extrapolation of seismicity models.

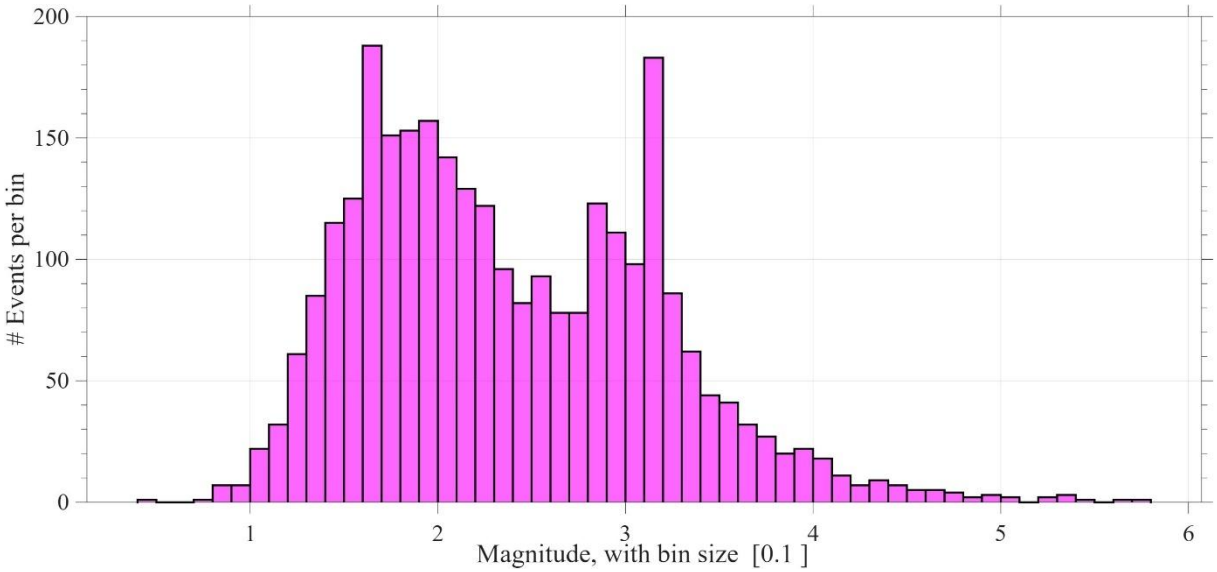


Figure 4. Magnitude histogram of the analyzed catalog (bin size = 0.1, M_L).

The time–magnitude plot (Figure 5) reveals distinct temporal variations in the number and magnitude of reported earthquakes. In the earlier part of the catalog, only a limited number of events were recorded, and these are mostly of higher magnitudes (M_L > 4–5). The largest instrumental event, the 27 March 1975 earthquake (M_L 5.7), is clearly identifiable and serves as a benchmark within the historical record. In contrast, from the late 1990s onward, the number of reported earthquakes increases substantially and extends to lower magnitudes. This shift primarily reflects improvements in seismic network density, data transmission, and instrumental sensitivity rather than a genuine change in the regional earthquake generation rate. The more frequent detection of small events (M_L ≈ 1–3) after 2000 improves the catalog's resolution for statistical analyses, particularly for estimating completeness (M_c) and b-value distributions. Accordingly, the time–magnitude pattern indicates that the catalog attains reliable completeness only in the modern instrumental era.

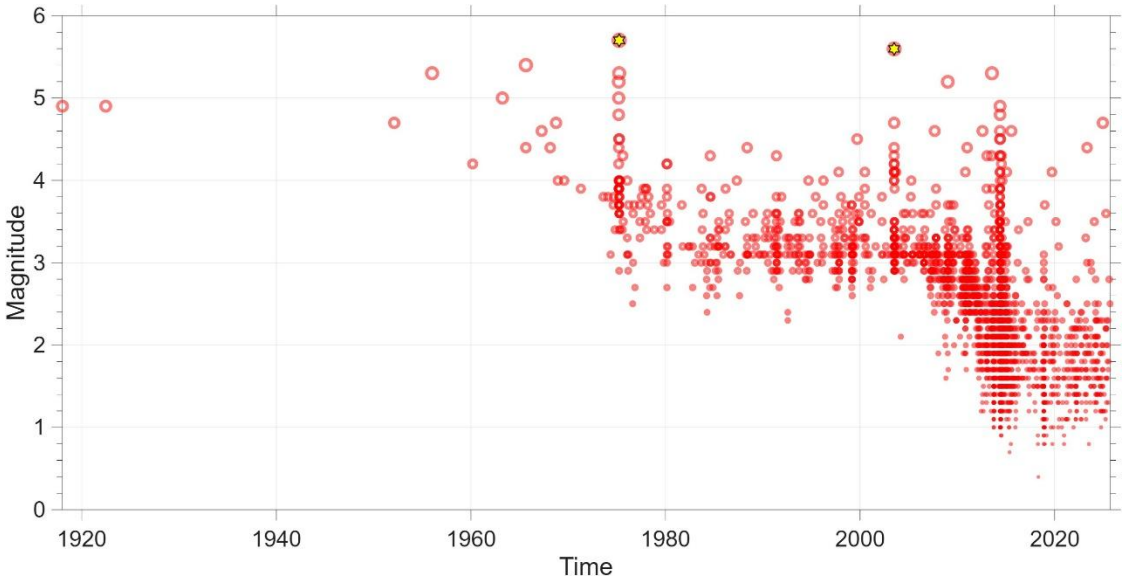


Figure 5. Time–magnitude distribution of the study-area earthquakes (M_L); a star highlights the 27 March 1975 event (M_L 5.7).

Before estimating seismicity parameters, the catalog was declustered to reduce the influence of dependent events (foreshocks/aftershocks) and better represent background seismicity. Declustering was performed using the Reasenberg (1985) approach, as implemented in ZMAP v. 7.1 [42], using the same parameter set reported in the Methods: look-ahead times of 1 day (unclustered) and 10 days (clustered), confidence level 0.95, XK factor = 0.5, interaction radius factor 10, effective minimum magnitude cutoff 1.5, epicentral error 1.5 km, and depth error 2 km. The Reasenberg declustering identified 88 spatiotemporal clusters comprising 1212 events out of 2855 in the study catalog (≈42%). Accordingly, 1643 events were classified as independent (background) seismicity and used for rate-based statistics and Gutenberg–Richter analyses. Equivalent events did not replace clusters; instead, dependent events were excluded from statistical calculations to reduce bias due to short-lived aftershock sequences. All rate-based calculations and Gutenberg–Richter analyses were conducted using the declustered catalog, unless explicitly stated otherwise.

Declustering is a critical step for estimating frequency–magnitude statistics, b-values, and recurrence intervals because it minimizes temporal dependence that can otherwise bias slope estimates in the Gutenberg–Richter relationship. Consistent with the declustering outcome, dependent events constitute a substantial fraction of the catalog, yet a large number of independent events (N = 1643) remain to characterize background rates robustly. The selected clustered look-ahead time (10 days) was adopted to capture the most intense portion of short-term aftershock activity expected for the magnitude range observed in this catalog (up to ML ≈ 5.7), while limiting the artificial linking of temporally distant events that could over-suppress background seismicity. The cumulative number of independent events over time (Figure 6) further illustrates the stable background activity after the removal of dependent clusters.

Figure 6 illustrates the cumulative number of earthquakes through time for the declustered catalog spanning 1917–2025. The cumulative curve shows a steady overall increase throughout the observation period, with the 27 March 1975 event (ML 5.7) highlighted by a star. Between approximately 1975 and the late 1990s, the cumulative number of events rises gradually, reflecting relatively sparse instrumental coverage and moderate seismic activity. After about 2000, the cumulative count increases more sharply, corresponding to the period of expanded seismic network density and improved detection sensitivity in the region. This higher slope in the cumulative curve primarily reflects enhanced recording capability rather than a sudden increase in the physical earthquake generation rate. Such trends are commonly observed in Turkish and Aegean seismic catalogs, where the transition to dense digital instrumentation around the early 2000s markedly improved detection thresholds.

The accelerated accumulation of detected events toward the end of the record indicates that the catalog is more complete in recent decades, particularly for small-magnitude earthquakes. This interpretation is quantitatively verified in the subsequent magnitude-of-completeness (M_c) analysis (Figure 7), which examines the temporal evolution of detection capability.

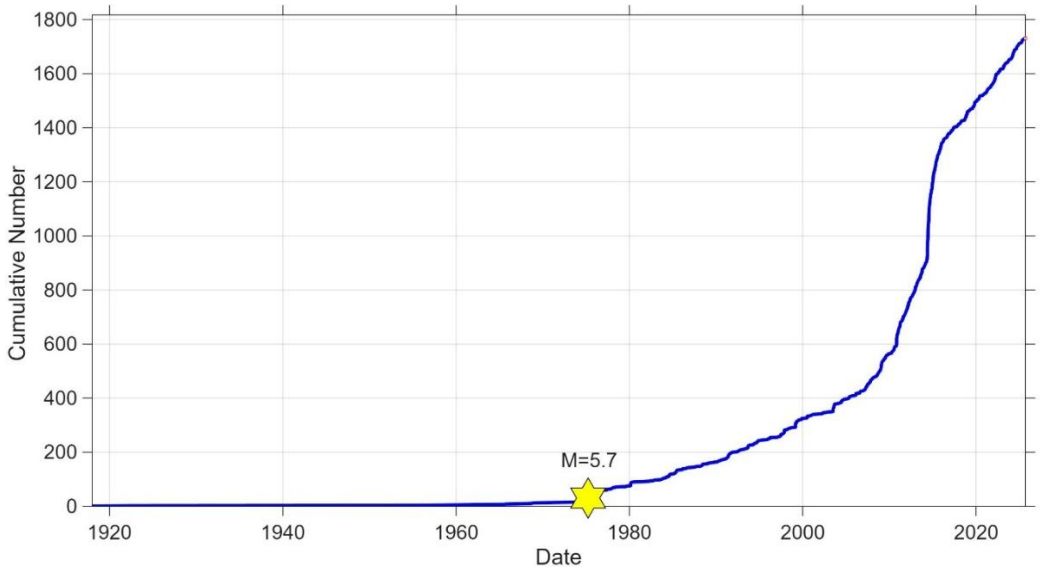


Figure 6. Cumulative number of earthquakes versus time for the declustered catalog; a star marks the 27 March 1975 event (M_L 5.7).

Figure 7 presents the temporal variation of the magnitude of completeness (M_c) estimated from the declustered catalog using a moving time window and the McBestCombo method implemented in ZMAP V. 7.1 [42]. Because the early part of the catalog is characterized by sparse reporting, the time-dependent completeness analysis $M_c(t)$ is reported only for the modern instrumental period (from 1975 onward), where event rates are sufficient to provide stable moving-window estimates. For the time-dependent M_c analysis, a window size of 100 events, a minimum of 100 events per window, 4% window overlap, and 200 bootstrap resamples were used; the magnitude binning was set to 0.1, with a smoothing parameter of 5. The choice of N = 100 represents a compromise between temporal resolution and statistical stability. This sample size is sufficient for robust McBestCombo estimates with bootstrap-based uncertainty bounds. It also allows tracking temporal changes in completeness. This is especially relevant after the network improvements of the late 1990s and the sharp transition after ~2010. Setting the minimum number of events equal to the window size ensures that each M_c estimate is based on the same sample size. This prevents poorly constrained windows during early or low-activity periods. It also improves the internal consistency of the $M_c(t)$ series. In the McBestCombo approach implemented in ZMAP, M_c is estimated using a composite ('best-combination') criterion that incorporates the maximum-curvature (MAXC) estimate—where M_c corresponds to the peak magnitude bin of the non-cumulative frequency–magnitude histogram—together with a goodness-of-fit (GFT) criterion, in which M_c is selected as the smallest cutoff magnitude for which the Gutenberg–Richter relation provides an acceptable fit to the observed FMD (commonly at the 90% level). The uncertainty bounds (δM_c) were

quantified via bootstrap resampling of each moving window [42, 63, 64]. Over the analysed period (1975 onward), M_c is highest in the mid-to-late 1970s, typically around ~3.6–3.8, and decreases rapidly to ~3.2 by the early 1980s. From the mid-1980s through approximately 2010, M_c remained remarkably stable at approximately 3.1–3.2. Since about 2010, M_c exhibits an abrupt decrease, reaching ~1.6–2.0 by 2014–2015, and thereafter fluctuates around ~1.6–1.8. The dashed curves in Figure 7 show the variability bounds (δM_c) associated with the moving-window estimates, illustrating the uncertainty range of the completeness level, which widens noticeably after ~2010, in parallel with the sharp transition in M_c.

This temporal trend reflects the progressive densification and modernization of the Turkish seismic network, particularly the deployment of broadband digital instrumentation after the late 1990s. The overall decrease in M_c through time indicates a lowering of the detection threshold for small-magnitude events, consistent with the steeper slope in cumulative counts (Figure 6). The mild variability in M_c after 2010 likely represents both improved network sensitivity and temporal fluctuations in operational coverage. Overall, the McBestCombo results demonstrate that the catalog is statistically complete for earthquakes with $M_L \geq$ ~3.1–3.2 since the mid-1980s and for events with $M_L \geq$ ~1.6–2.0 in the most recent decade, providing a reliable basis for subsequent frequency–magnitude and b-value analyses. For consistency across the whole study period, a single representative completeness threshold of $M_c = 3.2$ is therefore adopted. This value is consistent with the McBestCombo estimate from the declustered FMD (Figure 8) and helps ensure that the frequency, magnitude and b-value estimates are not biased by incomplete reporting at lower magnitudes in the earlier decades. M_c systematically decreases toward the present, consistent with improved detection capability. Differences in a-values primarily reflect the dependence of rates on the observation window and the adopted completeness threshold.

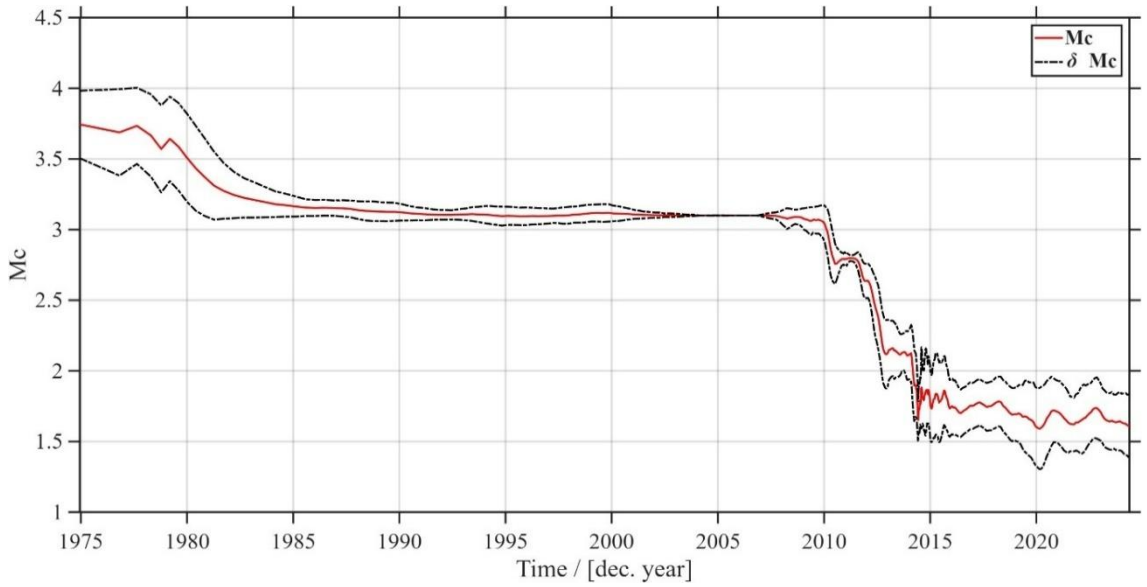


Figure 7. Temporal variation of the magnitude of completeness (M_c) estimated from the declustered catalog using a moving time window; dashed lines indicate the variability bounds (δM_c).

Based on the time–magnitude distribution and the time-dependent M_c estimates, the frequency–magnitude distribution (FMD) was evaluated for the declustered catalog. Figure 8 shows the cumulative and discrete forms of the FMD for three declustered analysis windows: (a) 1917–2025, (b) 1985–2025, and (c) 2010–2025. Panel (d) presents the original (non-declustered) 1917–2025 catalog to illustrate the influence of aftershock clustering on the frequency–magnitude distribution. For the entire catalog (1917–2025; Figure 8a), the completeness threshold was determined to be $M_c = 3.2$. Gutenberg–Richter parameters were then calculated for events with $M \geq M_c$, yielding a b-value of 0.91 ± 0.05 and an a-value of 5.392 (annualized a = 3.360). The fitted Gutenberg–Richter line for $M \geq 3.2$ is displayed in Figure 8a. Unless stated otherwise, the Gutenberg–Richter parameters discussed throughout the manuscript refer to the entire catalog (1917–2025; $M_c = 3.2$; Figure 8a), whereas the 1985–2025 and 2010–2025 results are presented to illustrate the influence of variations in temporal completeness.

Although a single conservative completeness threshold (M_c = 3.2) is adopted for the full 1917–2025 catalog to ensure long-term statistical consistency, the analyses for 1985–2025 and 2010–2025 demonstrate that b-values vary within a relatively limited range (0.91–1.06) and remain within the typical variability observed for segmented strike-slip systems despite progressively lower M_c values in recent decades. This multi-window comparison serves as a sensitivity test. It indicates that the inferred magnitude–frequency scaling is not strongly affected by improvements in detectability within uncertainty limits. However, the observed differences in b-values between time windows may reflect not only changes in completeness level (M_c), but also potential temporal variations in seismicity rates and stress conditions, which cannot be fully disentangled from completeness effects. The conservative M_c choice primarily affects the inclusion of smaller, more recent events without significantly altering the estimated b-value within the uncertainty limits.

To assess the influence of temporal changes in catalog completeness, the analysis time window was varied to evaluate sensitivity to this parameter (Figure 8b–c). For 1985–2025 (Figure 8b), the completeness threshold decreases to M_c = 2.9, with b = 1.06 ± 0.05 and a = 5.752 (annualized a = 4.143). For the more recent period 2010–2025 (Figure 8c), M_c further decreases to 2.3, yielding b = 0.92 ± 0.04 and a = 4.698 (annualized a = 3.503). Because the analysed time spans differ across windows, annualized a-values are not interpreted as directly comparable absolute rates between panels; instead, they illustrate the sensitivity of rate parameters to the selected observation window and completeness level.

The obtained b-value for the entire catalog (0.91 ± 0.05; Figure 8a) is close to the global average (~1.0) typically observed in active strike-slip environments (Scholz, 2015). However, being slightly below 1, it indicates a relative enrichment of larger events compared with a perfectly "unity" b-value case (b ≈ 1), i.e., a somewhat higher proportion of moderate-to-large events relative to small events. Considering the three-time windows together (b = 0.91–1.06; Figure 8a–c), the magnitude–frequency scaling is broadly consistent within uncertainty bounds. The obtained values also fall within the range commonly reported for segmented strike-slip fault systems. Minor differences may reflect both improved detectability and genuine temporal variability in seismic behavior. In the westernmost NAFZ and the Saros–NE Aegean transition zone, this near-unity b-value range is compatible with spatially and temporally variable fault-zone properties and stress conditions. It is also consistent with previously reported variability in b-value along the NAFZ. Similar b-values around unity (including $b < 1$ and $b \gtrsim 1$) have been reported for other NAFZ segments. They are commonly discussed in terms of variations in stress level, fault maturity, and structural heterogeneity, relative to segments that show systematically higher b-values [46, 65]. Comparable moderate-to-low b-values have also been documented in the western Marmara region, where spatial variations in b are evaluated together with Coulomb stress changes and regional stress conditions [66]. This consistency suggests that the Saros segment exhibits a magnitude–frequency scaling behavior compatible with the broader Marmara–NAFZ framework.

The entire catalog a-value of 5.392 (annualized a = 3.360) indicates moderate seismic productivity for the analysed region under the adopted completeness level ($M_c \approx 3.2$) and the declustering scheme. Because a-values are sensitive to both the observation time window and the completeness threshold (as illustrated by the 1985–2025 and 2010–2025 results in Figure 8b–c), these estimates are primarily used here as a consistent reference rather than as a strict comparison of absolute long-term rates across periods.

A direct comparison between the declustered (Figure 8a) and original (non-declustered; Figure 8d) 1917–2025 catalogs indicates that clustering mainly increases the total event count (reflected in higher a-values), whereas the slope of the frequency–magnitude relation (b-value) remains similar within overlapping uncertainty ranges. However, a slight decrease is observed in the non-declustered catalog (b = 0.91 ± 0.05 for the declustered catalog versus b = 0.85 ± 0.03 for the original catalog). This suggests that aftershock sequences primarily influence rate-based parameters and may introduce minor variations in the estimated slope, but do not fundamentally alter the overall magnitude–frequency scaling pattern within statistical uncertainty. Consequently, declustering is essential to derive background seismicity rates consistent with the Poisson independence assumption, and the comparison further indicates that the inferred scaling behavior is reasonably robust, though not entirely insensitive, to the treatment of clustering.

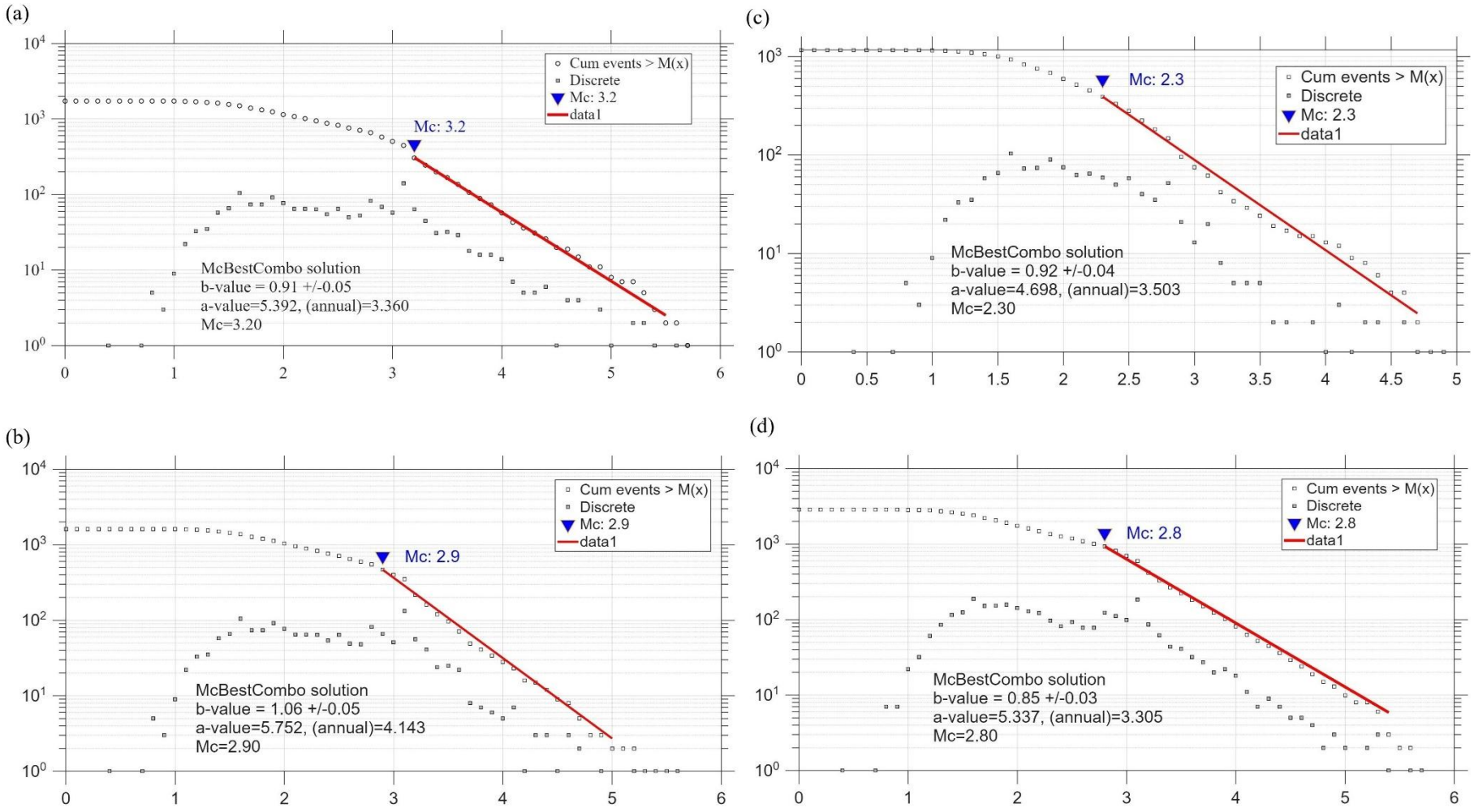


Figure 8. Frequency–magnitude distributions (FMDs) of the declustered catalog for (a) 1917–2025, (b) 1985–2025, (c) 2010–2025 and (d) the original (non-declustered) 1917–2025 catalog. Cumulative and discrete FMDs are shown together with the McBestCombo completeness magnitude (M_c, blue triangle) and the Gutenberg–Richter fit for $M \geq M_c$ (red line).

Together, the derived a- and b-values provide a consistent quantitative basis for the recurrence and probability calculations presented below and for comparison with other NAFZ segments. Recent instrumental detectability has been markedly improved (lower M_c in Figure 8c). Nevertheless, the entire declustered catalog (1917–2025) is used as the reference window. This choice ensures long-term characterization of background seismicity while preserving sampling of moderate-to-large events that control the high-magnitude tail relevant to recurrence assessment. To limit bias from time-varying reporting capability, a conservative completeness threshold (M_c = 3.2) is applied in the reference analysis, ensuring methodological consistency across the full observation period. The 1985–2025 and 2010–2025 results (Figure 8b–c) are presented mainly as sensitivity checks, demonstrating that the inferred b-values remain within a relatively narrow range and are consistent with the typical variability observed in strike-slip systems. However, minor fluctuations may reflect both evolving detectability and genuine temporal variability in seismic activity.

Figure 9 presents the recurrence-time (Figure 9a) and annual-probability (Figure 9b) curves calculated for three declustered catalog periods—1917–2025, 1985–2025, and 2010–2025—together with the original (non-declustered) 1917–2025 catalog. These curves were derived from the corresponding Gutenberg–Richter parameters and illustrate both temporal variations in seismic detectability and the influence of aftershock clustering on recurrence estimates within the Saros segment.

For the declustered 1917–2025 catalog, which represents the most statistically stable reference period ($b = 0.91 \pm 0.05$; $a = 5.392$; $M_c = 3.2$), recurrence intervals increase from approximately 5 years at $M_L = 4.5$ (annual probability $\approx 1.7 \times 10^{-1}$) to ~125 years at $M_L = 6.0$ and ~360 years at $M_L = 6.5$.

The 1985–2025 period, reflecting improved monitoring density and lower completeness ($M_c = 2.9$; $b = 1.06$; $a = 5.752$), shows shorter recurrence times for small-to-moderate magnitudes ($M_L < 5.0$) primarily attributable to enhanced detection capability and the corresponding increase in recorded event counts.

The 2010–2025 window ($M_c = 2.3$; $b = 0.92$; $a = 4.698$) represents the high-resolution modern instrumental era. Because this interval spans only 15 years, recurrence estimates for $M_L \geq 5.5$ are associated with greater statistical uncertainty due to limited sampling. They should therefore be interpreted as indicative rather than definitive measures of long-term recurrence.

All curves are truncated at $M_L = 6.5$ to avoid distortions related to local-magnitude saturation. Accordingly, recurrence values approaching the upper-magnitude limit ($M_L \approx 6.0$–6.5) should be interpreted as first-order approximations rather than strict maximum-magnitude constraints. Extrapolation beyond the largest observed magnitude (M_L 5.7) should be interpreted with caution, as it relies solely on the fitted Gutenberg–Richter relation and does not incorporate independent constraints on the maximum expected magnitude.

The comparison between the declustered and original (non-declustered) 1917–2025 curves shows that clustering systematically increases the apparent recurrence frequency across the magnitude range, resulting in shorter recurrence intervals when temporal dependence is not removed. At $M_L \approx 6.0$, the recurrence interval decreases from ~125 years (declustered) to ~75 years in the original catalog, and at $M_L \approx 6.5$ from ~360 years to ~150 years. Because recurrence intervals are exponentially related to the Gutenberg–Richter parameters, even modest differences in b-value and event counts produce substantial divergence at larger magnitudes; however, part of this divergence also reflects parameter uncertainty inherent in finite catalogs. These results indicate that declustering provides a more appropriate approximation of background seismicity rates under the Poisson independence assumption used in recurrence modeling.

Taken together, the results suggest that clustering primarily reflects short-term aftershock sequences and can bias long-term rate estimates if not explicitly addressed. For this reason, the declustered 1917–2025 catalog is used as the principal reference window for recurrence assessment in this study.

The adoption of a fixed completeness threshold ($M_c = 3.2$) for the reference analysis represents a deliberate trade-off between statistical homogeneity and information gain from recent instrumental improvements. While lower M_c values in the modern period would allow inclusion of additional small-magnitude events, applying time-dependent thresholds across the full catalog would introduce temporal inconsistency due to heterogeneous reporting capability. By prioritizing long-term comparability, the

derived seismicity parameters are interpreted as reflecting intrinsic background behavior rather than short-term detectability enhancements.

Because the spatial window of this study is relatively restricted (~0.3° × 0.9°) and contains a finite number of events, further subdivision for spatial M_c estimation would substantially reduce sample sizes and compromise the statistical stability of both M_c and b-value calculations. For this reason, the spatial variability of M_c was not separately modeled, and the analysis focuses on a statistically robust domain-wide estimate.

Accordingly, the 1985–2025 and 2010–2025 curves are retained as complementary short-term references illustrating temporal stability and monitoring effects. Interpreted together, the three periods indicate that the Saros segment maintains moderate but persistent seismic activity, with no statistically resolvable evidence, within the limits of the instrumental record, for systematic temporal change in the recurrence of larger events.

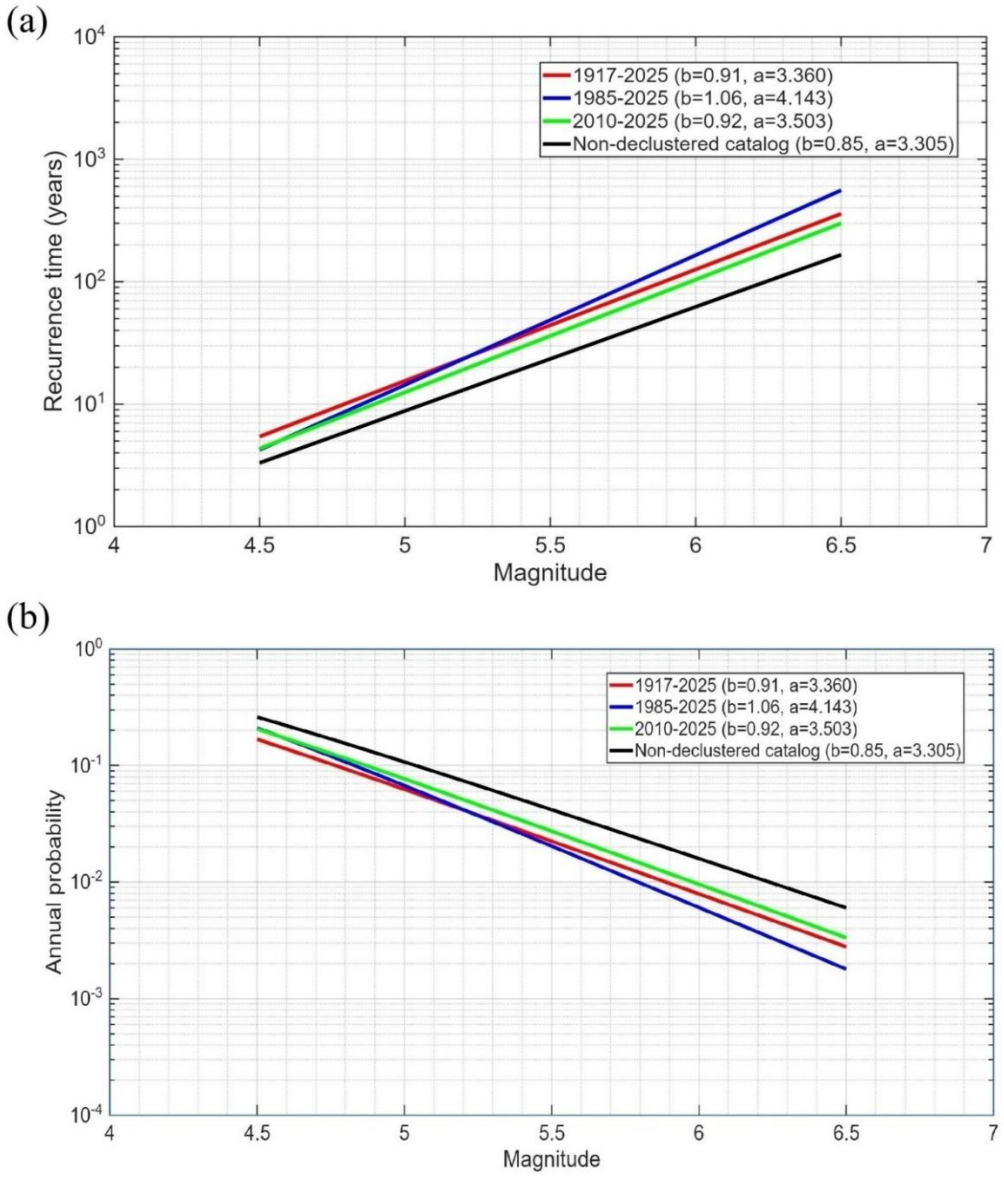


Figure 9. (a) Recurrence time and (b) annual probability versus magnitude computed from the Gutenberg–Richter parameters for three declustered catalog periods (1917–2025, 1985–2025, and 2010–2025) together with the original (non-declustered) 1917–2025 catalog. The comparison illustrates the influence of aftershock clustering on recurrence estimates. Curves are truncated at M_L = 6.5 to avoid local-magnitude saturation effects.

Focal mechanism results are summarized in Figures 10 and 11. Figure 10 presents the ternary (P–T–B axis plunge) distribution of the available solutions, with symbol size scaled by local magnitude ($M_L \approx$ 4.0–5.8) and color indicating focal depth (≈7–28 km). The mechanisms occupy a broad range of axis plunges, with most solutions falling within the strike-slip field and fewer extending toward the normal and reverse domains. This distribution suggests that strike-slip faulting dominates seismogenic deformation, consistent with the regional kinematic framework of the NAFZ. In contrast, the presence of a few normal or reverse components likely reflects local variations in stress orientation or fault geometry, or mechanical heterogeneity within the fault zone under transtensional conditions.

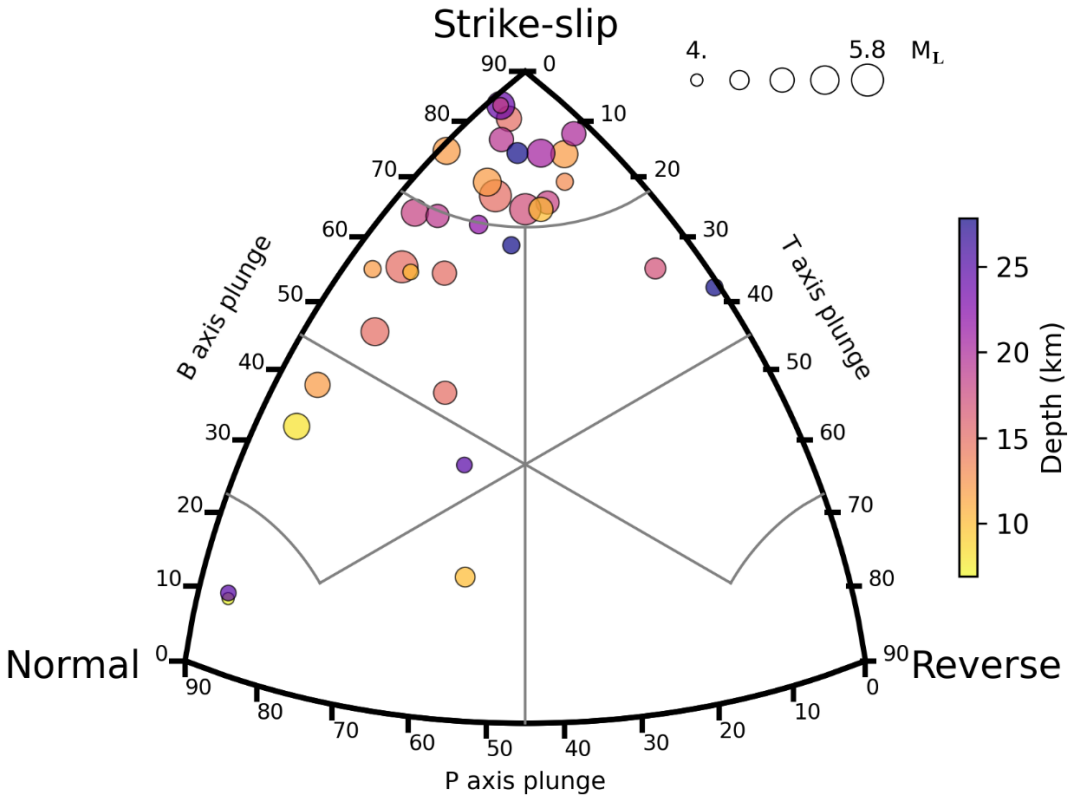


Figure 10. Ternary (P–T–B axis plunge) plot of focal mechanism solutions; symbol size scales with M_L and color indicates depth (km).

Figure 11 shows the spatial distribution of the same 33 focal mechanisms within the study area. The solutions are predominantly offshore, and they closely follow the mapped fault traces (black lines). The strike-slip solutions are well aligned with the ENE–WSW-trending main strand of the NAFZ, supporting a dextral sense of motion. Minor normal components observed in several events indicate localized extensional deformation, consistent with the transtensional nature of the Saros segment and its mechanical linkage to the northern Aegean domain. Together, these observations suggest a broadly coherent regional stress regime dominated by dextral strike-slip motion, although local departures from pure strike-slip behavior are evident. This first-order stress pattern is further quantified in the following section through stress-tensor inversion.

Stress tensor inversion results are summarized in Figure 12. Figure 12a shows the orientations of the three principal stress axes obtained from the inversion. The best-fitting stress tensor is defined by the following azimuth/plunge pairs: σ_1 = 280.66°/8.22°, σ_2 = 86.14°/81.52°, and σ_3 = 190.36°/2.10°. Figure 12b presents the corresponding orientation distributions for σ_1, σ_2, and σ_3, while Figure 12c illustrates the estimated stress shape ratio (R = 0.4679).

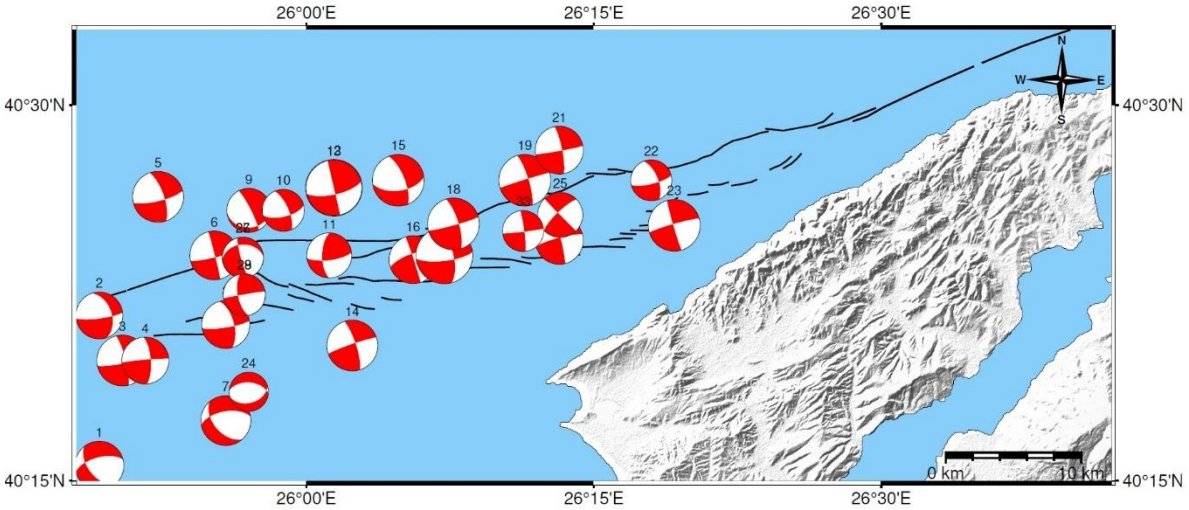


Figure 11. Map of 33 focal mechanism beachballs in the study area; numbers label individual solutions, and black lines show mapped fault traces. Focal mechanism solutions were compiled from the AFAD catalog, the GCMT database, the RCMT catalog, the ISC, and published studies (see Data and Methods section for details).

The nearly horizontal WNW–ESE σ_1 axis and steeply plunging σ_2 axis indicate a strike-slip stress regime consistent with the regional dextral kinematics of the NAFZ. The low plunge of σ_3 (≈2°) indicates a near-horizontal extension direction roughly N–S, which aligns with the transtensional character of the Saros region and reflects its structural linkage to the northern Aegean domain, where N–S-oriented extension dominates the present-day stress field. The stress ratio R = 0.47 suggests a moderate difference between the intermediate and maximum principal stresses, reflecting a relatively balanced strike-slip regime rather than a strongly compressional or extensional state. This also suggests that the intermediate principal stress (σ_2) plays a transitional rather than a dominant role. Physically, this ratio indicates a mechanically sensitive equilibrium regime. In such a regime, the local stress field can readily fluctuate between pure strike-slip and transtensional configurations in response to subtle variations in the orientation of σ_2. When R values approach ~0.5, the stress state is particularly responsive to minor perturbations—such as changes in local fault geometry, lithological contrasts, or pore-fluid pressure—that can modulate the balance between horizontal shear and vertical extension. In the Saros segment, this sensitivity manifests as localized variations in fault kinematics along the northern margin of the basin, where WNW–ESE compression (σ_1) and nearly horizontal N–S extension (σ_3) coexist. Consequently, the observed R = 0.47 value confirms a dextral strike-slip regime with a subordinate extensional component and identifies the Saros domain as a stress-transition corridor linking the westernmost NAF to the northern Aegean extensional system.

Overall, the stress tensor inversion supports a dextral strike-slip regime with a minor extensional component, consistent with the focal mechanism solutions and the regional kinematic framework. These results indicate that the Saros segment likely represents a mechanically continuous transition between the westernmost NAFZ and the extensional domain of the northern Aegean. A comparable integration of focal-mechanism solutions and Coulomb stress evaluations for the western Marmara region has similarly highlighted the role of mixed strike-slip and extensional deformation under the present stress regime [66]. This consistency further supports the interpretation of the Saros segment as part of the Marmara–Saros–North Aegean transition zone.

Previous studies have shown that Gutenberg–Richter b-values vary systematically with tectonic stress state and faulting style, even though the relation is not strictly deterministic [46, 67-69]. At regional to global scales, b-values commonly decrease with increasing differential stress; accordingly, normal-faulting environments tend to exhibit the highest b-values, strike-slip regimes intermediate values, and reverse/thrust settings the lowest values [67-69]. More recent studies further suggest that earthquake size distributions should be interpreted as multivariate, because the observed b-value may also depend

on depth, structural heterogeneity, fault roughness, and fault maturity [70-73]. Although both parameters are discussed in relation to tectonic regime, the Gutenberg–Richter b-value and the stress shape ratio R do not describe the same physical quantity. The b-value reflects the statistical distribution of earthquake sizes, whereas R characterizes the relative magnitudes of the principal stresses inferred from focal mechanisms. Accordingly, their correspondence should be interpreted only at the level of tectonic compatibility, not as a one-to-one predictive relationship. Within this framework, the Saros b-values (0.91–1.06, with a reference value of 0.91 ± 0.05) are compatible with a strike-slip-dominant tectonic setting locally modified by transtensional deformation.

Taken together, the Gutenberg–Richter parameters and stress inversion results indicate that the Saros segment functions as an actively deforming transtensional transition zone rather than a passive termination of the North Anatolian Fault Zone. The reference b-value of 0.91 ± 0.05, derived from the full 1917–2025 catalog (M_c = 3.2), indicates a stable magnitude–frequency scaling with a slightly enhanced proportion of moderate-to-large events relative to a unity (b ≈ 1) distribution. Across all tested time windows (1917–2025, 1985–2025, and 2010–2025), b remains within 0.91–1.06. This range falls within the typical variability reported for strike-slip systems, despite improved instrumental detectability over time. Recurrence estimates for M_L ≈ 6.0 events, together with the inferred strike-slip-dominant stress regime (R = 0.47), are consistent with ongoing tectonic deformation under the current regional stress configuration. However, stress accumulation rates cannot be directly quantified from the present analysis. Although local magnitude saturation limits extrapolation toward larger magnitudes, the long-term catalog shows persistent seismic productivity. Therefore, within the broader Marmara–North Aegean framework, the Saros transition zone can be interpreted as a structurally continuous and seismically responsive corridor that warrants consideration in future seismic hazard evaluations.

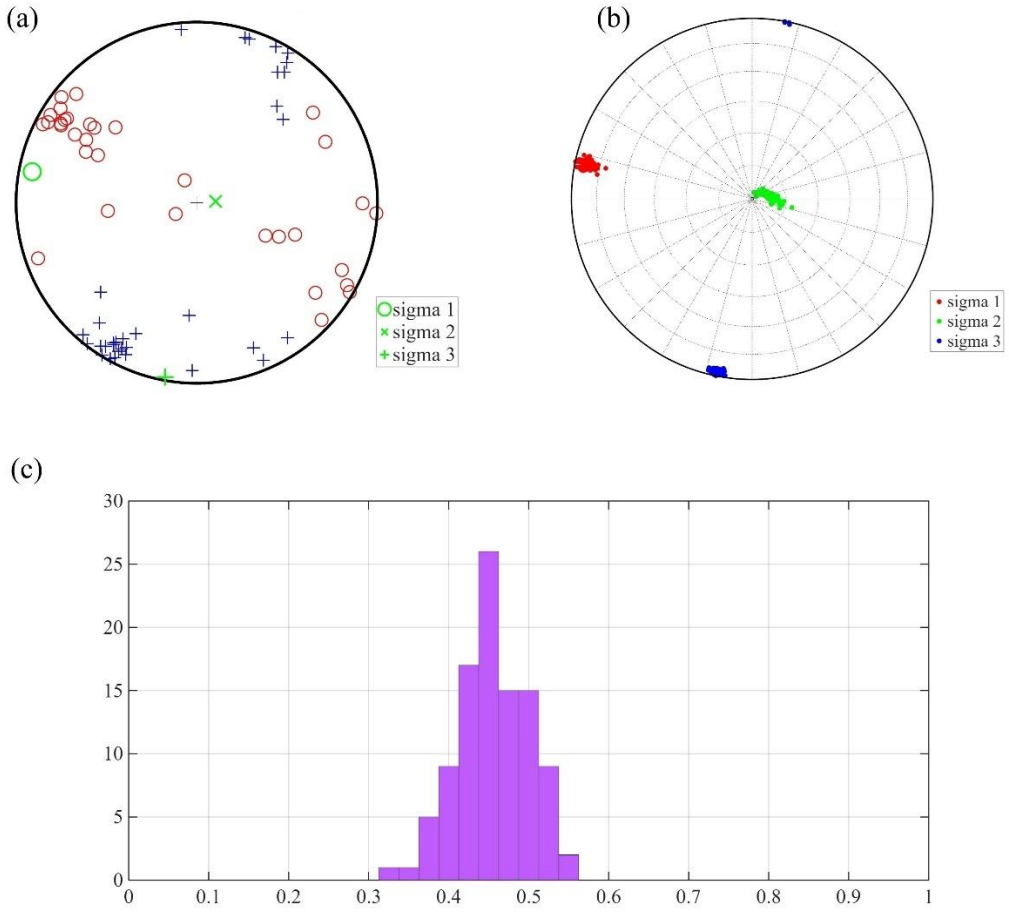


Figure 12. Stress tensor inversion results: (a) lower-hemisphere projection of principal stress axes (σ1, σ2, and σ3); (b) polar distributions of axis orientations; (c) histogram of the stress shape ratio R.

5. CONCLUSION

This study provides a spatially restricted and completeness-controlled integration of seismicity statistics and stress-field analysis for the westernmost segment of the North Anatolian Fault Zone within the Saros transition domain. By constructing a homogenized and declustered M_L-based catalog (1917–2025) and systematically evaluating completeness variability, the analysis demonstrates internally consistent magnitude–frequency scaling and temporally stable recurrence behavior across instrumental subperiods. These results indicate that the apparent increase in seismicity during recent decades primarily reflects improved detectability rather than a fundamental change in tectonic loading conditions.

Stress tensor inversion and focal mechanism classification reveal a dominantly dextral strike-slip regime with a subordinate N–S extensional component, defining a mechanically transitional stress configuration between the western NAFZ and the northern Aegean extensional province. The inferred stress ratio and principal stress orientations indicate that deformation in the Saros segment is governed by coupled shear and extension rather than by a purely strike-slip or purely extensional regime.

In light of previous studies linking lower b-values to relatively higher differential stress and showing systematic differences among normal, strike-slip, and reverse tectonic regimes, the Saros reference b-value (0.91 ± 0.05) is consistent with a strike-slip-dominant setting locally modified by transtension [46, 67-69]. At the same time, because b-value may also be influenced by depth, heterogeneity, fault roughness, and fault maturity, this agreement is interpreted as evidence of tectonic consistency rather than a direct deterministic relationship between b-value and the stress ratio R [70-73].

By combining magnitude-frequency characteristics, recurrence stability, focal-mechanism patterns, and stress geometry within the defined study area, the Saros segment is interpreted as a mechanically coherent transform-transtensional linkage zone rather than a passive structural termination of the NAFZ. Accordingly, the correspondence between $b \approx 0.91$ and $R \approx 0.47$ is taken to indicate a literature-supported compatibility between seismic scaling and stress regime, rather than a direct deterministic relationship. Although the instrumental record limits resolution in the upper-magnitude range and local-magnitude saturation constrains strict maximum-magnitude inference, the declustered long-term catalog provides a statistically robust first-order characterization of background seismicity. The derived parameterization refines the process-level understanding of fault interaction and stress partitioning in the Marmara-Saros-North Aegean transition and establishes a consistent basis for regional seismic hazard assessment and segmentation models.

Data Availability

The earthquake dataset utilized in this study includes both instrumental and historical seismicity, compiled from various publicly available national and international sources. Instrumental earthquake data were obtained from the KOERI earthquake catalog (https://www.koeri.boun.edu.tr/sismo/2/earthquake-catalog/; accessed January 2026).

Historical earthquake information was compiled from the AFAD historical earthquake database (https://deprem.afad.gov.tr/event-historical; accessed January 2026).

Focal mechanism solutions were retrieved from the GCMT catalog (https://www.globalcmt.org; accessed January 2026), the RCMT catalog (http://rcmt2.bo.ingv.it; accessed January 2026), and the International Seismological Centre (ISC) database (https://www.isc.ac.uk; accessed January 2026).

All processed and derived datasets produced in this study—including the homogenized local magnitude (M_L) catalog, declustered seismicity data, magnitude-of-completeness estimates, Gutenberg–Richter parameters, recurrence metrics, and stress inversion outputs—can be obtained from the corresponding author upon reasonable request.

Statement of Research and Publication Ethics

The study is complied with research and publication ethics.

Artificial Intelligence (AI) Contribution Statement

ChatGPT (OpenAI) was used to improve the manuscript's language and readability. No new data were generated, and the tool did not draw any scientific conclusions. The author reviewed and edited the manuscript and accepts full responsibility for the final content.

REFERENCES

[1] J. Fraser, J. Pigati, A. Hubert-Ferrari, K. Vanneste, U. Avsar, and S. Altınok, "A 3000-Year Record of Ground-Rupturing Earthquakes along the Central North Anatolian Fault near Lake Ladik, Turkey," Bull. Seismol. Soc. Am., vol. 99, pp. 2681–2703, 10/01/2009, doi: 10.1785/0120080024.

[2] A. Barka, "The North Anatolian fault zone," in Final meeting of IGCP Project 206 A worldwide comparison of the characteristics of major active faults (Mammoth Lakes, 1989-07-02), 1992, pp. 164–195.

[3] J. F. Dewey and A. M. C. Şengör, "Aegean and surrounding regions: Complex multiplate and continuum tectonics in a convergent zone," GSA Bulletin, vol. 90, no. 1, pp. 84–92, 1979, doi: 10.1130/0016-7606(1979)90<84: AASRCM>2.0.CO;2.

[4] H. Karabulut et al., "A source study of the 6 July 2003 (M_w 5.7) earthquake sequence in the Gulf of Saros (Northern Aegean Sea): Seismological evidence for the western continuation of the Ganos fault," Tectonophysics, vol. 412, no. 3, pp. 195–216, 2006/01/20/ 2006, doi: https://doi.org/10.1016/j.tecto.2005.09.009.

[5] C. Yaltırak, "Tectonic evolution of the Marmara Sea and its surroundings," Mar. Geol., vol. 190, no. 1, pp. 493–529, 2002/10/15/ 2002, doi: 10.1016/S0025-3227(02)00360-2.

[6] M. Nakano, S. Citak, and D. Kalafat, "Focal mechanism determinations of earthquakes along the North Anatolian fault, beneath the Sea of Marmara and the Aegean Sea," Earth, Planets and Space, vol. 67, no. 1, p. 159, 2015/09/28 2015, doi: 10.1186/s40623-015-0330-z.

[7] O. Tatar et al., "Palaeomagnetic evidence for the neotectonic evolution of the Erzincan Basin, North Anatolian Fault Zone, Turkey," J. Geodyn., vol. 65, pp. 244–258, 2013/04/01/ 2013, doi: https://doi.org/10.1016/j.jog.2012.03.009.

[8] R. S. Stein, J. H. Dieterich, and A. A. Barka, "Role of stress triggering in earthquake migration on the North Anatolian fault," Phys. Chem. Earth., vol. 21, no. 4, pp. 225–230, 1996/07/01/ 1996, doi: https://doi.org/10.1016/S0079-1946(97)00039-6.

[9] A. Amemoutou, P. Martínez-Garzón, V. Durand, G. Kwiatek, M. Bohnhoff, and G. Dresen, "Spatio-temporal variations of seismic coupling along a transform fault: the western North Anatolian Fault Zone," Geophys. J. Int., vol. 235, no. 2, pp. 1982–1995, 2023, doi: 10.1093/gji/ggad341.

[10] Barka et al., "The Surface Rupture and Slip Distribution of the 17 August 1999 Izmit Earthquake (M 7.4), North Anatolian Fault," Bull. Seismol. Soc. Am., vol. 92, pp. 43–60, 02/01 2002, doi: 10.1785/0120000841.

[11] A. Pinar, Y. Honkura, and K. Kuge, "Seismic activity triggered by the 1999 Izmit earthquake and its implications for the assessment of future seismic risk," Geophys. J. Int., vol. 146, no. 1, pp. F1–F7, 2001, doi: 10.1046/j.0956-540x.2001.01476.x.

[12] M. Aksoy et al., "Subaqueous fault scarps of the North Anatolian Fault in the Gulf of Saros (NE Aegean); where is the western limit of the 1912 Mürefte-Şarköy earthquake rupture?" Geophys. J. Int., pp. 589–604, 04/01 2022, doi: 10.1093/gji/ggab462.

[13] E. Mantovani, M. Viti, C. Tamburelli, D. Babbucci, M. Baglione, and V. D'Intinosante, "Seismicity Patterns in Some Mediterranean Zones After the 1939 Anatolian Earthquake: Insights on Seismic Risk and the Tectonic Setting," GeoHazards, vol. 6, no. 2, p. 29doi: 10.3390/geohazards6020029.

[14] L. C. McNeill, A. Mille, T. A. Minshull, J. M. Bull, N. H. Kenyon, and M. Ivanov, "Extension of the North Anatolian Fault into the North Aegean Trough: Evidence for transtension, strain partitioning, and analogues for Sea of Marmara basin models," Tectonics, vol. 23, no. 2, 2004, doi: https://doi.org/10.1029/2002TC001490.

[15] Ö. Emre et al., "Active fault database of Turkey," Bull. Earthquake Eng., vol. 16, no. 8, pp. 3229–3275, 2018/08/01 2018, doi: 10.1007/s10518-016-0041-2.

[16] P. Wessel et al., "The Generic Mapping Tools Version 6," Geochem. Geophys. Geosyst., vol. 20, no. 11, pp. 5556–5564, 2019, doi: 10.1029/2019GC008515.

[17] I. Lazos, S. Sboras, and C. Pikridas, "Tectonic Geodesy Synthesis and Review of the North Aegean Region, Based on the Strain Patterns of the North Aegean Sea, Strymon Basin and Thessalian Basin Case Studies," Applied Sciences, vol. 13, no. 17, p. 9943, 2023. [Online]. Available: https://www.mdpi.com/2076-3417/13/17/9943.

[18] S. Barbot and J. R. Weiss, "Connecting subduction, extension and shear localization across the Aegean Sea and Anatolia," Geophys. J. Int., vol. 226, no. 1, pp. 422–445, 2021, doi: 10.1093/gji/ggab078.

[19] V. Saltogianni, M. Gianniou, T. Taymaz, S. Yolsal-Çevikbilen, and S. Stiros, "The 2014 M_w 6.9 North Aegean Trough (Nat) Earthquake: Seismological and Geodetic Evidence," Bulletin of the Geological Society of Greece, vol. 50, no. 3, pp. 1583–1592, 07/27 2016, doi: 10.12681/bgsg. 11877.

[20] M. Aksoy, "The 9 August 1912 Mürefte-Şarköy earthquake of the North Anatolian fault," Mediterranean Geoscience Reviews, vol. 3, pp. 1–20, 03/01 2021, doi: 10.1007/s42990-021-00050-z.

[21] M. Aksoy, M. Vallée, and Z. Çakir, "Rupture characteristics of the AD 1912 Murefte (Ganos) earthquake segment of the North Anatolian Fault (western Turkey)," Geology, vol. 38, pp. 991–994, 11/01 2010, doi: 10.1130/G31447.1.

[22] C. Yaltırak and B. Alpar, "Kinematics and evolution of the northern branch of the North Anatolian Fault (Ganos Fault) between the Sea of Marmara and the Gulf of Saros," Mar. Geol., vol. 190, no. 1, pp. 351–366, 2002/10/15/2002, doi: https://doi.org/10.1016/S0025-3227(02)00354-7.

[23] C. Yaltırak, B. Alpar, and H. Yüce, "Tectonic elements controlling the evolution of the Gulf of Saros (northeastern Aegean Sea, Turkey)," Tectonophysics, vol. 300, no. 1, pp. 227–248, 1998/12/31/ 1998, doi: https://doi.org/10.1016/S0040-1951(98)00242-X.

[24] M. Aksoy et al., "Paleoseismology of the Ganos segment; the western extent of the North Anatolian Fault (Turkey)," Turk. J. Earth Sci., vol. 32, pp. 380–401, 01/01 2023, doi: 10.55730/1300-0985.1850.

[25] M. Meghraoui, M. E. Aksoy, H. S. Akyüz, M. Ferry, A. Dikbaş, and E. Altunel, "Paleoseismology of the North Anatolian Fault at Güzelköy (Ganos segment, Turkey): Size and recurrence time of earthquake ruptures west of the Sea of Marmara," *Geochem. Geophys. Geosyst.*, vol. 13, no. 4, Art. no. Q04005, Apr. 2012, doi: 10.1029/2011GC003960..

[26] R. Armijo, N. Pondard, B. Meyer, G. Uçarkuş, B. Mercier de Lépinay, J. Malavieille, S. Dominguez, M.-A. Gutscher, S. Schmidt, C. Beck, N. Çağatay, Z. Çakır, C. İmren, K. Eriş, B. Natalin, S. Özalaybey, L. Tolun, I. Lefèvre, L. Seeber, L. Gasperini, C. Rangin, Ö. Emre, and K. Sarıkavak, "Submarine fault scarps in the Sea of Marmara pull-apart (North Anatolian Fault): Implications for seismic hazard in Istanbul," *Geochem. Geophys. Geosyst.*, vol. 6, no. 6, Art. no. Q06009, Jun. 2005, doi: 10.1029/2004GC000896.

[27] D. Vardar, "Evidence for active faulting in the eastern part of the Gulf of Saros, northern Aegean, from high-resolution seismic data," J. Earth Syst. Sci., vol. 128, no. 3, p. 52, 2019/02/25, doi: 10.1007/s12040-019-1084-y.

[28] I. Sianko et al., "A practical probabilistic earthquake hazard analysis tool: case study Marmara region," Bull. Earthquake Eng., vol. 18, no. 6, pp. 2523–2555, 2020/04/01 2020, doi: 10.1007/s10518-020-00793-4.

[29] C. Wollin, M. Bohnhoff, P. Martínez-Garzón, L. Küperkoch, and C. Raub, "A unified earthquake catalogue for the Sea of Marmara Region, Turkey, based on automatized phase picking and travel-time inversion: Seismotectonic implications," Tectonophysics, vol. 747-748, pp. 416–444, 2018/11/13/ 2018, doi: https://doi.org/10.1016/j.tecto.2018.05.020.

[30] T. Ustaömer et al., "Faulting, mass-wasting and deposition in an active dextral shear zone, the Gulf of Saros and the NE Aegean Sea, NW Turkey," Geo-Mar. Lett., vol. 28, no. 3, pp. 171–193, 2008/06/01 2008, doi: 10.1007/s00367-007-0099-6.

[31] G. Beyhan, A. Keskinsezer, and A. Silahtar, "Sismik Yansıma ve Gravite Verilerinden Saros Körfezinin Temel Yapısının İncelenmesi," SAÜ Fen Bilimleri Enstitüsü Dergisi, vol. 21, pp. 1–1, 04/01 2017, doi: 10.16984/saufenbilder.284225.

[32] M. Rodriguez et al., "Evolution of the North Anatolian Fault from a diffuse to a localized shear zone in the North Aegean Sea during the Plio-Pleistocene," Geophys. J. Int., vol. 235, no. 3, pp. 2614–2639, 2023, doi: 10.1093/gji/ggad364.

[33] A. M. Dziewonski, T. A. Chou, and J. H. Woodhouse, "Determination of earthquake source parameters from waveform data for studies of global and regional seismicity," J Geophys Res Solid Earth, vol. 86, no—B4, pp. 2825–2852, 1981/04/10 1981, doi: https://doi.org/10.1029/JB086iB04p02825.

[34] G. Ekström, M. Nettles, and A. M. Dziewoński, "The global CMT project 2004–2010: Centroid-moment tensors for 13,017 earthquakes," Phys. Earth Planet. Inter., vol. 200-201, pp. 1–9, 2012/06/01/ 2012, doi: https://doi.org/10.1016/j.pepi.2012.04.002.

[35] European-Mediterranean Regional Centroid-Moment Tensors Catalog (RCMT), Istituto Nazionale di Geofisica e Vulcanologia (INGV), 2002.

[36] J. Quinteros et al., "The GEOFON program in 2020," Seismol. Res. Lett., vol. 92, no. 3, pp. 1610–1622, 2021.

[37] S. Castellaro, F. Mulargia, and Y. Y. Kagan, "Regression problems for magnitudes," Geophys. J. Int., vol. 165, no. 3, pp. 913–930, 2006, doi: 10.1111/j.1365-246X.2006.02955.x.

[38] R. Das et al., "Earthquake Magnitude Conversion Problem," Bull. Seismol. Soc. Am., vol. 108, no. 4, pp. 1995–2007, 2018, doi: 10.1785/0120170157.

[39] B. Lolli and P. Gasperini, "A comparison among general orthogonal regression methods applied to earthquake magnitude conversions," Geophys. J. Int., vol. 190, no. 2, pp. 1135–1151, 2012, doi: 10.1111/j.1365-246X.2012.05530.x.

[40] H. R. Wason, R. Das, and M. L. Sharma, "Magnitude conversion problem using general orthogonal regression," Geophys. J. Int., vol. 190, no. 2, pp. 1091–1096, 2012, doi: 10.1111/j.1365-246X.2012.05520.x.

[41] P. Reasenberg, "Second-order moment of central California seismicity, 1969–1982," J Geophys Res Solid Earth, vol. 90, no. B7, pp. 5479–5495, 1985, doi: https://doi.org/10.1029/JB090iB07p05479.

[42] S. Wiemer, "A Software Package to Analyze Seismicity: ZMAP," Seismol. Res. Lett., vol. 72, no. 3, pp. 373–382, 2001, doi: 10.1785/gssrl. 72.3.373.

[43] B. Gutenberg and C. F. Richter, "Frequency of earthquakes in California," Bull. Seismol. Soc. Am., vol. 34, no. 4, pp. 185–188, 1944, doi: 10.1785/bssa0340040185.

[44] K. Mogi, "Study of Elastic Shocks Caused by the Fracture of Heterogeneous Materials and its Relations to Earthquake Phenomena," 1962.

[45] C. Scholz, "The frequency-magnitude relation of microfracturing in rock and its relation to earthquakes," Bull. Seismol. Soc. Am., vol. 58, no. 1, pp. 399–415, 1968, doi: 10.1785/bssa0580010399.

[46] C. Scholz, "On the stress dependence of the earthquake b value," Geophys. Res. Lett., vol. 42, no. 5, pp. 1399–1402, 2015, doi: https://doi.org/10.1002/2014GL062863.

[47] C. Frohlich and S. D. Davis, "Teleseismic b values; Or, much ado about 1.0," J Geophys Res Solid Earth, vol. 98, no. B1, pp. 631–644, 1993, doi: https://doi.org/10.1029/92JB01891.

[48] K. Aki, "Maximum likelihood estimate of b in the formula log N = a-bM and its confidence limits," Bull. Earthq. Res. Inst. Tokyo Univ, vol. 43, pp. 237–239, 1965.

[49] C. A. Cornell, "Engineering seismic risk analysis," Bull. Seismol. Soc. Am., vol. 58, no. 5, pp. 1583–1606, 1968.

[50] J. Greenhough and I. Main, "A Poisson model for earthquake frequency uncertainties in seismic hazard analysis," Geophys. Res. Lett., vol. 35, 07/15 2008, doi: 10.1029/2008GL035353.

[51] B. Orlecka-Sikora and S. Lasocki, "Interval Estimation of Seismic Hazard Parameters," Pure Appl. Geophys., vol. 174, no. 3, pp. 779–791, 2017/03/01 2017, doi: 10.1007/s00024-016-1419-4.

[52] C. Frohlich and K. D. Apperson, "Earthquake focal mechanisms, moment tensors, and the consistency of seismic activity near plate boundaries," Tectonics, vol. 11, no. 2, pp. 279–296, 1992, doi: https://doi.org/10.1029/91TC02888.

[53] Y. Y. Kagan, "Double-couple earthquake focal mechanism: random rotation and display," Geophys. J. Int., vol. 163, no. 3, pp. 1065–1072, 2005, doi: 10.1111/j.1365-246X.2005.02781.x.

[54] A. N. Kaverina, A. V. Lander, and A. G. Prozorov, "Global Creepex Distribution and Its Relation to Earthquake-Source Geometry and Tectonic Origin," Geophys. J. Int., vol. 125, no. 1, pp. 249–265, 1996, doi: 10.1111/j.1365-246X.1996.tb06549.x.

[55] J. A. Álvarez-Gómez, "FMC—Earthquake focal mechanisms data management, cluster and classification," SoftwareX, vol. 9, pp. 299–307, 2019/01/01/ 2019, doi: https://doi.org/10.1016/j.softx.2019.03.008.

[56] A. Bala, D. Toma-Danila, and M. Radulian, "Focal mechanisms in Romania: statistical features representative for earthquake-prone areas and spatial correlations with tectonic provinces," Acta Geodaetica et Geophysica, vol. 54, no. 2, pp. 263–286, 2019/06/01 2019, doi: 10.1007/s40328-019-00260-w.

[57] A. J. Michael, "Determination of stress from slip data: Faults and folds," J Geophys Res Solid Earth, vol. 89, no. B13, pp. 11517–11526, 1984, doi: https://doi.org/10.1029/JB089iB13p11517.

[58] A. J. Michael, "Use of focal mechanisms to determine stress: A control study," J Geophys Res Solid Earth, vol. 92, no. B1, pp. 357–368, 1987, doi: https://doi.org/10.1029/JB092iB01p00357.

[59] A. K. Mutlu, "Seismicity, focal mechanism, and stress tensor analysis of the Simav region, western Turkey," Open Geosciences, vol. 12, no. 1, pp. 479–490, 2020, doi: doi:10.1515/geo-2020-0010.

[60] D. Delvaux and A. Barth, "African stress pattern from formal inversion of focal mechanism data," Tectonophysics, vol. 482, no. 1, pp. 105–128, 2010/02/25/ 2010, doi: https://doi.org/10.1016/j.tecto.2009.05.009.

[61] V. Vavryčuk, "Iterative joint inversion for stress and fault orientations from focal mechanisms," Geophys. J. Int., vol. 199, no. 1, pp. 69–77, 2014, doi: 10.1093/gji/ggu224.

[62] C. Christova and T. Tsapanos, "Depth distribution of stresses in the Hokkaido Wadati-Benioff zone as deduced by inversion of earthquake focal mechanisms," J. Geodyn., vol. 30, no. 5, pp. 557–573, 2000/12/01/ 2000, doi: https://doi.org/10.1016/S0264-3707(00)00009-0.

[63] S. Wiemer and M. Wyss, "Minimum Magnitude of Completeness in Earthquake Catalogs: Examples from Alaska, the Western United States, and Japan," Bull. Seismol. Soc. Am., vol. 90, no. 4, pp. 859–869, 2000, doi: 10.1785/0119990114.

[64] S. Wiemer and M. Wyss, "Mapping spatial variability of the frequency-magnitude distribution of earthquakes," in Advances in Geophysics, vol. 45, R. Dmowska and B. Saltzman Eds.: Elsevier, 2002, pp. 259–V.

[65] S. Öztürk, "Characteristics of seismic activity in the Western, Central and Eastern parts of the North Anatolian Fault Zone, Turkey: Temporal and spatial analysis," Acta Geophys., vol. 59, no. 2, pp. 209–238, 2011/04/01 2011, doi: 10.2478/s11600-010-0050-5.

[66] H. Alkan, S. Öztürk, Ö. Bektaş, and A. Büyüksaraç, "Statistical and seismotectonic analyses of the Marmara region under existing stress regime in the west of the NAFZ," Acta Geophys., vol. 73, no. 2, pp. 1117–1136, 2025/04/01 2025, doi: 10.1007/s11600-024-01449-6.

[67] L. Gulia and S. Wiemer, "The influence of tectonic regimes on the earthquake size distribution: A case study for Italy," Geophys. Res. Lett., vol. 37, no. 10, 2010, doi: https://doi.org/10.1029/2010GL043066.

[68] D. Schorlemmer, S. Wiemer, and M. Wyss, "Variations in earthquake-size distribution across different stress regimes," Nature, vol. 437, no. 7058, pp. 539–542, 2005/09/01 2005, doi: 10.1038/nature04094.

[69] Y.-M. Wu, S. K. Chen, T.-C. Huang, H.-H., Huang, W.-A., Chao and I. Koulakov, "Relationship Between Earthquake b-Values and Crustal Stresses in a Young Orogenic Belt," Geophys. Res. Lett., vol. 45, no. 4, pp. 1832–1837, 2018/02/28 2018, doi: https://doi.org/10.1002/2017GL076694.

[70] T. H. W. Goebel, G. Kwiatek, T. W. Becker, E. E. Brodsky, and G. Dresen, "What allows seismic events to grow big?: Insights from b-value and fault roughness analysis in laboratory stick-slip experiments," Geology, vol. 45, no. 9, pp. 815–818, 2017, doi: 10.1130/G39147.1.

[71] M. Kozlowska, M. Brudzinski, P. Friberg, R. Skoumal, N. Baxter, and B. Currie, "Maturity of nearby faults influences seismic hazard from hydraulic fracturing," Proceedings of the National Academy of Sciences, vol. 115, p. 201715284, 02/05 2018, doi: 10.1073/pnas. 1715284115.

[72] A. Petruccelli et al., "Simultaneous Dependence of the Earthquake-Size Distribution on Faulting Style and Depth," Geophys. Res. Lett., vol. 46, no. 20, pp. 11044–11053, 2019/10/28 2019, doi: https://doi.org/10.1029/2019GL083997.

[73] E. A. Al-Heety and O. J. Mohammad, "The Reliance of the Earthquake B-Value on Depth and Focal Mechanism," Iraqi Geological Journal, vol. 54, no. 1D, pp. 1–10, 2021.